

A SIMPLE GPU-ACCELERATED SOLVER FOR THE SCHRÖDINGER OPERATOR WITH APPLICATIONS TO GROUND STATES AND HAMILTONIAN SIMULATION

XINYU LIU* AND XIANGXIONG ZHANG†

Abstract. We extend the tensor-product direct solver from the Laplacian to the Schrödinger operator $-\Delta + V$. When the potential V_1 is separable, the operator $-\Delta + V_1$ is inverted or exponentiated at cost $O(N^{1+1/d})$ in d dimensions via per-axis eigendecomposition. On a single NVIDIA A100 GPU, this costs less than one second for 10^9 degrees of freedom in 3D. For non-separable potentials $V = V_1 + V_2$, the same solver provides a preconditioner $(-\Delta + V_1)^{-1}$ for the preconditioned conjugate gradient (PCG) method and a propagator for operator-splitting time integrators. For bounded V_2 , we prove that the preconditioned operator has a bounded condition number and a clustered spectrum with at most finitely many outlier eigenvalues, independently of the mesh size, and also independently of the domain size when V_1 is a confining potential. This explains the mesh- and domain-independent PCG iteration counts observed in practice. We apply this method to ground state computation via inverse iteration for linear problems and via the a_u gradient flow for Gross–Pitaevskii energy in 3D, and also Hamiltonian simulation via the approximated qHOP and Magnus-2 splitting methods from 3D to 9D on a single NVIDIA GH200 GPU.

Key words. tensor-product spectral method, GPU computing, Schrödinger equation, Gross–Pitaevskii equation, Strang splitting, Yoshida splitting

AMS subject classifications. 65M70, 65N35, 65F15, 81-08, 35Q55, 81Q05

1. Introduction. It is well known that the discrete Laplacian on Cartesian meshes has a tensor-product structure, which can be used as a simple and fast direct solver since the 1960s [29, 18, 33, 25, 28]. For a general potential V , this structure is lost for the Schrödinger operator $-\Delta + V$. In this paper, we extend the tensor-product solver from the Laplacian to the Schrödinger operator $-\Delta + V$ as follows. For a separable potential $V_1(\mathbf{x}) = \sum_k f_k(x_k)$, the operator $-\Delta + V_1$ can still be inverted or exponentiated via per-axis eigendecomposition at cost $O(N^{1+1/d})$ with $O(N)$ memory. For non-separable potentials $V = V_1 + V_2$, the tensor-product solver provides a preconditioner $(-\Delta + V_1)^{-1}$ for the preconditioned conjugate gradient (PCG) method and a propagator for operator-splitting time integrators. For bounded V_2 , we prove that the preconditioned operator $(-\Delta + V_1)^{-1}(-\Delta + V_1 + V_2)$ has a bounded condition number and a clustered spectrum with at most finitely many outliers, independently of the mesh size (Theorem 3.4), and also independently of the domain size when V_1 is a confining potential (Theorem 3.5). This can explain mesh- and domain-independent PCG iteration counts observed in numerical tests for suitable potentials. Similar to the simple GPU acceleration of the direct inversion of the Laplacian in [28], we show that the Schrödinger operator $-\Delta + V$ can be easily inverted on GPU (Sections 2–3), e.g., it takes less than 1 second for inverting $-\Delta + V_1$ for one billion DoFs on one Nvidia GPU such as A100 and GH200.

Fast inversion of the Schrödinger operator has several applications. We first consider ground state computation (Section 4): for separable potentials via shifted inverse iteration, and for non-separable potentials via shifted inverse iteration with PCG, preconditioned by $(-\Delta + V_1)^{-1}$. We also demonstrate that the defocusing Gross–Pitaevskii ground state via the a_u flow can be easily implemented in 3D on a

*Department of Mathematics, The Ohio State University, 231 West 18th Avenue, Columbus, OH 43210 (liu.12165@osu.edu).

†Corresponding author. Department of Mathematics, Purdue University, 150 N. University Street, West Lafayette, IN 47907 (zhan1966@purdue.edu).

single GPU.

Another application is Hamiltonian simulation. If (λ_1, u_1) is the ground state eigenpair of $H = -\Delta + V$, then $\psi(x, t) = e^{-i\lambda_1 t} u_1(x)$ is an exact solution of the time-dependent Schrödinger equation $i\partial_t \psi = H\psi$. We use this stationary solution as a reference for testing operator-splitting methods (Sections 5–6).

In the quantum computing literature, two recent splitting methods have been considered for simulating $i\partial_t \psi = (A+B)\psi$ in the interaction picture, where A has large spectral norm but can be fast-forwarded (e.g., $A = -\Delta$ via QFT). The *quantum Highly Oscillatory Protocol* (qHOP) [1] approximates the first-order Magnus expansion and achieves $O(\Delta t^2)$ superconvergence with an error preconstant independent of problem size n [1]. The *Magnus-2* algorithm [12] uses the second-order Magnus expansion and achieves $O(\Delta t^4)$ superconvergence [12, 7]. On a quantum computer, the matrix exponential of a sum of interaction-picture Hamiltonians is implemented via linear combination of unitaries (LCU). Classically, this cannot be computed directly at large n . We implement an approximate version using a product formula where each factor is computed exactly via tensor-product propagations and a pointwise multiplication (equation (5.2) and Remark 5.1 in Section 5.2). We test these methods for multi-body Coulomb Hamiltonians in 4D, 6D, and 9D (Section 6). The approximated versions of qHOP and Magnus-2 are tested in multiple dimensions for two purposes. First, these tests can serve as a verification of their theoretical superconvergence orders in high dimensions. Since the approximated versions introduce additional product-formula errors beyond the original splitting error, observing the predicted convergence orders despite these additional errors provides supporting numerical evidence for the original schemes. Second, the same product-formula implementation yields a family of classical splitting methods with parameter M : $M = 1$ recovers the classical Strang and Yoshida splittings, while $M \geq 3$ reduces the error constant at the same convergence order, demonstrating that qHOP and Magnus-2 can serve as improved classical integrators compared to standard schemes. Furthermore, as a classical numerical scheme, the splitting $A = -\Delta + V_1$, $B = V_2$ gives smaller errors than $A = -\Delta$, $B = V_1 + V_2$ (Tables 7 and 8 in Section 5).

In related work, the tensor-product approach to Schrödinger equations has been explored by Caliri et al. [8], whose μ -mode integrator exploits Kronecker structure for 3D problems at $\sim 2 \times 10^6$ DoFs. GPU acceleration for Schrödinger simulation has also been explored in [16]. The split-step spectral method was introduced in [5]. We refer to [26, 24] for reviews of semiclassical methods and to [23, 36, 21] for splitting error analysis and classical Magnus integrators. On the quantum computing side, gate complexity for real-space simulation of Schrödinger equations was established in [10], Trotter error bounds for interacting electrons were given in [35, 17], and quantum resource estimates for 2D Coulomb simulation are given in [15].

All results in this paper can be reproduced via Python (JAX) code available at <https://github.com/zhan1966/schrodinger>. GPU cards are available to many researchers through programs such as the NSF-funded ACCESS (Advanced Cyberinfrastructure Coordination Ecosystem: Services & Support) [6], which provides allocations on GPU clusters including NVIDIA A100 and GH200 nodes. The direct inversion of the tensor-structured Laplacian on A100 was demonstrated in [28, 9, 19]. This paper extends the same approach to the Schrödinger operator $-\Delta + V$. All computations in this paper require only a single GPU.

The rest of the paper is organized as follows. Section 2 describes the tensor-product spectral solver. Section 3 develops the PCG preconditioner and analyzes its mesh- and domain-independent condition number and spectral clustering. Section 4

presents ground state computation via shifted inverse iteration and Gross–Pitaevskii gradient flows. Sections 5 and 6 present Hamiltonian simulation results in 3D through 9D. Some concluding remarks are given in Section 7. Appendix A presents the Hermite spectral discretization on unbounded domains.

2. Direct solver for $-\Delta + V$ with a separable potential. The idea in this paper applies to any numerical method with a tensor-product structure on rectangular domains. For simplicity, throughout the paper we focus on the Q^k spectral element method (SEM), which is the high order finite element method with Q^k basis and $(k+1)$ -point Gauss-Lobatto quadrature. For $k=1$, it is the classical second order finite difference method. For $k \geq 2$, Q^k SEM can be proven to be a $(k+2)$ -th order finite difference scheme in ℓ^2 -norm over quadrature point values [27]. As an example of another suitable method, we also include a Hermite spectral method on unbounded domains in Appendix A. See also [28] for using Q^k SEM in a Poisson solver.

2.1. A direct solver via eigendecomposition for separable potentials. We consider the elliptic PDE

$$(2.1) \quad -\Delta u(\mathbf{x}) + V(\mathbf{x})u(\mathbf{x}) = b(\mathbf{x}), \quad \mathbf{x} \in \Omega,$$

on a rectangular domain $\Omega = [-L, L]^d$ (or on \mathbb{R}^d via Hermite functions in Appendix A). For simplicity, we consider the homogeneous Dirichlet boundary condition, and extensions of the scheme to homogeneous Neumann and periodic boundary conditions are straightforward. With the Q^k spectral element method using Gauss–Lobatto quadrature [27], let $K_d = M_d^{-1}S_d$ denote the 1D discrete Laplacian in direction $d \in \{x, y, z\}$, with M_d the mass matrix, S_d the stiffness matrix, and I_d the identity matrix. For Q^1 elements on a uniform mesh, K_d is the well-known tridiagonal $(-1, 2, -1)$ matrix from second order finite difference. Let n be the number of interior grid points in each direction. For any d -dimensional array X of size $n \times \dots \times n$, let $\text{vec}(X)$ denote the vector of size n^d obtained by reshaping all entries of X into a column vector. Then in 3D, the discretized system takes the form (see [28, 9]):

$$(2.2) \quad [I_z \otimes I_y \otimes K_x + I_z \otimes K_y \otimes I_x + K_z \otimes I_y \otimes I_x + \text{diag}(\text{vec}(V))] \text{vec}(U) = \text{vec}(B),$$

where V is the array of potential values $V(\mathbf{x}_i)$ at the grid points. When the potential is separable, $V(\mathbf{x}) = f_x(x) + f_y(y) + f_z(z)$, the potential matrix decomposes as $\text{diag}(\text{vec}(V)) = I_z \otimes I_y \otimes F_x + I_z \otimes F_y \otimes I_x + F_z \otimes I_y \otimes I_x$ with $F_d = \text{diag}(f_d(x_1), \dots, f_d(x_n))$, and the system (2.2) reduces to the Kronecker form

$$(2.3) \quad (I_z \otimes I_y \otimes H_x + I_z \otimes H_y \otimes I_x + H_z \otimes I_y \otimes I_x) \text{vec}(U) = \text{vec}(B),$$

where $H_d = K_d + F_d = M_d^{-1}S_d + F_d$ for each axis $d \in \{x, y, z\}$. Each H_d can be diagonalized by

$$(2.4) \quad H_d = M_d^{-1/2}(M_d^{-1/2}S_dM_d^{-1/2} + F_d)M_d^{1/2} = T_d\Lambda_dT_d^{-1},$$

where $T_d = M_d^{-1/2}Q_d$, $T_d^{-1} = Q_d^T M_d^{1/2}$, and $Q_d\Lambda_dQ_d^T$ is the eigendecomposition of the symmetric matrix $M_d^{-1/2}S_dM_d^{-1/2} + F_d$.

The solution is then computed in four steps:

1. Off-line setup (one-time): compute the eigendecomposition $H_d = T_d\Lambda_dT_d^{-1}$ for each axis d . Since H_d is an $n \times n$ matrix, this costs $O(n^3) = O(N)$.
2. Forward transform: apply $T_z^{-1} \otimes T_y^{-1} \otimes T_x^{-1}$ to B .

3. Solve the diagonal system: divide by $(\Lambda_x)_{ii} + (\Lambda_y)_{jj} + (\Lambda_z)_{kk}$.

4. Backward transform: apply $T_z \otimes T_y \otimes T_x$.

Steps 2 and 4 contain the dominant computational cost $\mathcal{O}(N^{4/3})$ for $N = n^3$. The memory cost is $\mathcal{O}(N)$.

The same factorization applies to the time-dependent Schrödinger propagator $e^{-i(-\Delta+V_1)\Delta t}$. Since $-\Delta+V_1 = T \Lambda T^{-1}$, where $T = T_z \otimes T_y \otimes T_x$ and Λ is the diagonal tensor of eigenvalue sums $\Lambda_{ijk} = (\Lambda_x)_{ii} + (\Lambda_y)_{jj} + (\Lambda_z)_{kk}$, the matrix exponential is

$$e^{-i(-\Delta+V_1)\Delta t} \psi = T (e^{-i\Lambda\Delta t} \odot (T^{-1} \psi)),$$

with \odot denoting pointwise multiplication. The only change from the direct inversion is that the eigenvalue division in step 3 is replaced by multiplication by $e^{-i\Lambda_{ijk}\Delta t}$. Steps 1, 2 and 4 are the same. Thus, once the eigendecomposition is computed, both the direct solve $(-\Delta + V_1)^{-1}b$ and the propagator $e^{-i(-\Delta+V_1)\Delta t}\psi$ cost $\mathcal{O}(N^{1+1/d})$.

2.2. Numerical tests. We demonstrate the solver on the equation

$$(2.5) \quad (-\Delta + V) u = f, \quad \mathbf{x} \in [-1, 1]^d.$$

For 3D, we use the non-isotropic separable potential

$$(2.6) \quad V(\mathbf{x}) = 1600 \left(\sin^2\left(\frac{\pi}{4}x\right) + \sin^2\left(\frac{\pi}{4}y\right) + \sin^2\left(\frac{\pi}{4}z\right) \right) + (x^2 + 2y^2 + 3z^2),$$

exact solution $u^* = \sin(\pi x) \sin(2\pi y) \sin(3\pi z)$, and $f = (-\Delta + V) u^*$. For 4D and 6D tests, we use the harmonic trapping potential $V(\mathbf{x}) = \sum_{k=1}^d x_k^2$, and the exact solution $u^* = \prod_{k=1}^d \sin(k\pi x_k)$.

All computations are implemented in Python with JAX, similar to the Python implementation in [28]. Table 1 reports *setup* time for offline eigendecomposition and eigenvalue array construction, and *solve* time for applying the direct solver, which would be the per-iteration cost in an iterative method such as PCG in later sections.

In Table 1, we also report different precision formats on a GH200 GPU (96 GB HBM3). FP32 (single precision) stores each number in 32 bits, using half the memory of FP64. TF32 (TensorFloat-32) uses 32-bit storage but performs matrix multiplications on GPU tensor cores at reduced precision for fast matrix operations. See [28] for more comparison of TF32 with FP32. BF16 (bfloat16) uses only 16 bits per number, further reducing memory and enabling larger grids on the same device, but with only ~ 3 -digit precision.

3. Efficient Inversion of $-\Delta + V$. When $V = V_1 + V_2$ contains a separable V_1 and a non-separable V_2 , we use PCG with the preconditioner $(-\Delta + V_1)^{-1}$.

3.1. Test potentials. We consider two physically motivated potentials.

(a) *Harmonic plus quartic potential* [3]:

$$(3.1) \quad V(x, y, z) = 2(1-\alpha)(\gamma_x x^2 + \gamma_y y^2) + \frac{\kappa}{2}(x^2 + y^2)^2 + \gamma_z z^2.$$

We consider $\gamma_x = \gamma_y = 1$, $\gamma_z = 3$, $\alpha = 1.4$, $\kappa = 0.3$, and we split $V = V_1 + V_2$ with separable part $V_1 = \gamma_x x^2 + \gamma_y y^2 + \gamma_z z^2$ and non-separable remainder

$$V_2 = (2(1-\alpha)-1)(\gamma_x x^2 + \gamma_y y^2) + \frac{\kappa}{2}(x^2 + y^2)^2 = -1.8(x^2 + y^2) + 0.15(x^2 + y^2)^2.$$

The quartic coupling $(x^2 + y^2)^2$ makes V_2 genuinely non-separable.

TABLE 1

Direct inversion of $(-\Delta + V)$ via Q^k SEM on Nvidia GH200 96 GB. 3D: potential (2.6), 4D/6D: $V = \sum x_k^2$. At matched n , solve times (in seconds) are identical across Q^k . In FP64, all three dimensions reach $\sim 10^9$ DoFs: $1099^3 \approx 1.3 \times 10^9$, $179^4 \approx 1.0 \times 10^9$, $33^6 \approx 1.3 \times 10^9$.

Precision	Dim	Q^k	N_{cell}	n	DoFs	Setup (s)	Solve (s)	ℓ^2 rel. err
FP64	3D	Q^1	1100	1099	1099^3	5.2	0.508	3.66×10^{-6}
		Q^2	550	1099	1099^3	5.1	0.512	1.93×10^{-9}
		Q^{10}	110	1099	1099^3	6.4	0.510	$7.66 \times 10^{-13\dagger}$
	4D	Q^{10}	18	179	179^4	6.2	0.195	$1.29 \times 10^{-13\dagger}$
	6D	Q^2	17	33	33^6	5.9	0.258	$2.95 \times 10^{-2§}$
FP32	3D	Q^2	500	999	999^3	5.4	0.270	7.17×10^{-7}
		Q^{10}	15	149	149^4	5.8	0.058	4.99×10^{-7}
		Q^{10}	20	199	199^4	5.8	0.188	$6.20 \times 10^{-7\dagger}$
	6D	Q^{10}	3	29	29^6	5.7	0.052	4.75×10^{-4}
TF32	3D	Q^2	500	999	999^3	6.6	0.133	5.13×10^{-4}
BF16	3D	Q^2	500	999	999^3	5.4	0.088	1.65×10^{-2}
		Q^2	800	1599	1599^3	5.6	0.517	1.64×10^{-2}

\dagger FP64 rounding floor. \ddagger FP32 rounding floor. \S Mesh too coarse for Q^2 to resolve $\prod_{k=1}^6 \sin(k\pi x_k)$.

(b) Harmonic plus stirrer potential [2, 22, 4]:

$$(3.2) \quad V(x, y, z) = \underbrace{\gamma_x^2 x^2 + \gamma_y^2 y^2 + \gamma_z^2 z^2}_{V_1} + \underbrace{2w_0 e^{-\delta((x-r_0)^2 + y^2)}}_{V_2},$$

with $\gamma_x = 1$, $\gamma_y = 1$, $\gamma_z = 2$, $w_0 = 4$, $\delta = 1$, $r_0 = 1$. This potential includes a harmonic trap with a localized Gaussian stirrer.

3.2. PCG for $-\Delta + V_1 + V_2$ (non-separable case). When $V = V_1 + V_2$ contains a non-separable component V_2 , the system $(-\Delta + V_1 + V_2)u = f$ cannot be solved directly by the tensor-product solver. We consider the preconditioned conjugate gradient (PCG) method. Antoine et al. [3] showed that PCG with the combined preconditioner $P_C = V^{-1/2}(-\Delta)^{-1}V^{-1/2}$ achieves grid-independent iteration counts. In this subsection, we show that the preconditioner $P = (-\Delta + V_1)^{-1}$ is stronger. It is applied by the tensor-product direct solver with a cost $O(N^{4/3})$ in 3D.

EXAMPLE 3.1 (PCG on bounded domain). We consider the quartic (3.1) and stirrer (3.2) potentials on $[-8, 8]^3$ with Q^6 SEM, Dirichlet BC, a random right-hand side f , FP32 arithmetic, on a GH200 GPU. In all FP32 PCG tests reported here, the offline eigendecomposition of $-\Delta + V_1$ is computed in FP64 and only then cast to lower precision for the online PCG iteration. Figure 1 shows the convergence at two grid sizes (197^3 and 701^3 DoFs). Both preconditioners exhibit grid-independent iteration counts. The proposed preconditioner converges in 33–38 iterations (quartic) and 5–6 iterations (stirrer), compared to 214–255 iterations with $(-\Delta)^{-1}$ for the quartic potential and ~ 375 iterations with $P_C = V^{-\frac{1}{2}}(-\Delta)^{-1}V^{-\frac{1}{2}}$ for the stirrer potential.

Figure 1 also shows that the performance of the preconditioner $(-\Delta + V_1)^{-1}$ is independent of both the domain size L and the mesh size h for the stirrer potential, while for the quartic potential, the iteration count grows with L .

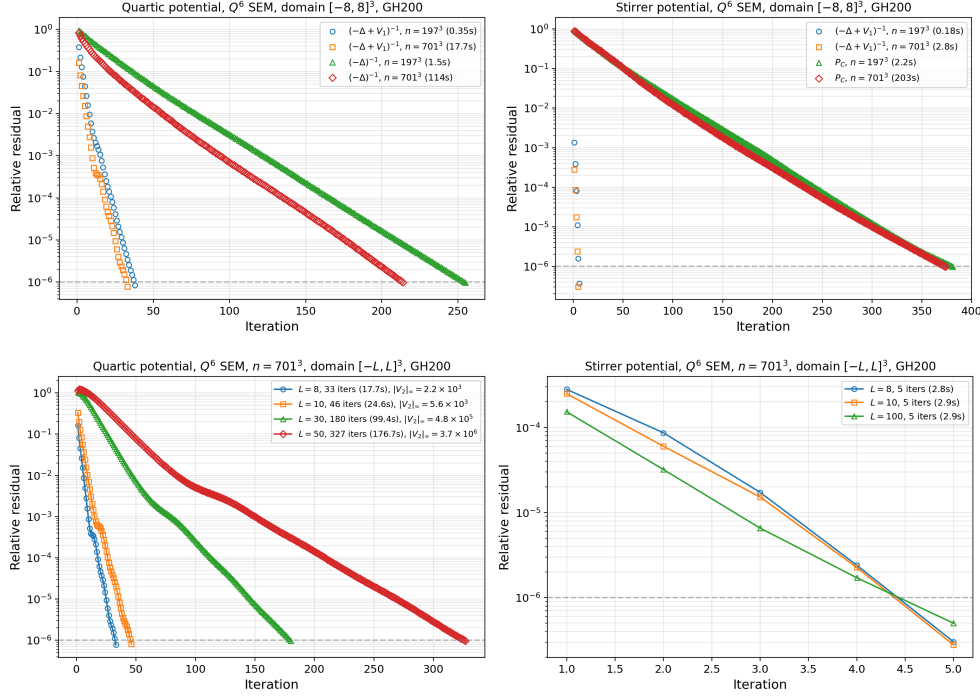


FIG. 1. PCG convergence (relative residual vs. iteration) for $(-\Delta + V_1 + V_2)u = f$, Q^6 SEM, FP32, GH200. Top row: quartic potential (3.1) (left) and stirrer potential (3.2) (right), both at $n = 701^3$, comparing the proposed preconditioner $(-\Delta + V_1)^{-1}$ with the $(-\Delta)^{-1}$ or P_C . Bottom row: domain dependence of $(-\Delta + V_1)^{-1}$ for the quartic potential (left, $L = 8, 10, 30, 50$) and the stirrer potential (right, $L = 8, 10, 100$). Total GPU time for each case is shown in the legend.

In the rest of this section, we explain this behavior by analyzing the spectrum of the preconditioned operator, which involves standard spectral theory for conforming finite element discretizations (such as Q^k SEM) under two assumptions on V_1 and V_2 .

Assumption I (bounded domain): $V_1 \in L^\infty(\Omega)$ with $V_1 \geq 0$, and $V_2 \in L^\infty(\Omega)$.

Assumption II (confining potential): $V_1 \geq 0$ with $V_1(x) \rightarrow \infty$ as $|x| \rightarrow \infty$ and $V_1 \in L^\infty_{\text{loc}}(\mathbb{R}^d)$, and $V_2 \in L^\infty(\mathbb{R}^d)$.

Assumption II is stronger since it implies Assumption I on any bounded domain Ω .

DEFINITION 3.1 (A -inner product). For a bounded domain $\Omega \subset \mathbb{R}^d$, under Assumption I, define the inner product for $H_0^1(\Omega)$:

$$\langle u, v \rangle_A = \int_{\Omega} (\nabla u \cdot \nabla v + V_1 u v) \, dx.$$

Since $V_1 \geq 0$ and $V_1 \in L^\infty(\Omega)$, the Poincaré inequality gives $(1 + C_P^2)^{-1} \|u\|_{H^1}^2 \leq \|u\|_A^2 \leq \max(1, \|V_1\|_{L^\infty}) \|u\|_{H^1}^2$, so $\|\cdot\|_A$ is equivalent to the standard H^1 norm.

DEFINITION 3.2 (Perturbation operators and Riesz map). Under the setting of Definition 3.1, let $X_h \subset H_0^1(\Omega)$ be a conforming finite element subspace with mesh parameter $h > 0$. Define:

- (a) The Riesz map $R : L^2(\Omega) \rightarrow H_0^1(\Omega)$ by $\langle Rf, v \rangle_A = (f, v)_{L^2}$ for all $v \in H_0^1(\Omega)$.

(b) The continuous perturbation operator $K : H_0^1(\Omega) \rightarrow H_0^1(\Omega)$ by

$$(3.3) \quad \langle Ku, v \rangle_A = \int_{\Omega} V_2 u v \, d\mathbf{x}, \quad \forall v \in H_0^1(\Omega).$$

- (c) $K_h : X_h \rightarrow X_h$ by $\langle K_h u_h, v_h \rangle_A = \int_{\Omega} V_2 u_h v_h \, d\mathbf{x}$ for all $v_h \in X_h$.
(d) The projection $\Pi_h : H_0^1(\Omega) \rightarrow X_h$ by $\langle \Pi_h u, v_h \rangle_A = \langle u, v_h \rangle_A$ for all $v_h \in X_h$.
(e) The Galerkin discretizations $-\Delta_h + V_{1,h}$ and $-\Delta_h + V_{1,h} + V_{2,h}$ on X_h :

$$((-\Delta_h + V_{1,h}) u_h, v_h)_{L^2} := \langle u_h, v_h \rangle_A,$$

$$((-\Delta_h + V_{1,h} + V_{2,h}) u_h, v_h)_{L^2} := \langle u_h, v_h \rangle_A + \int_{\Omega} V_2 u_h v_h \, d\mathbf{x},$$

for all $u_h, v_h \in X_h$. Here $V_{2,h}$ denotes the restriction of V_2 to X_h via the L^2 inner product, i.e., $(V_{2,h} u_h, v_h)_{L^2} = \int_{\Omega} V_2 u_h v_h \, d\mathbf{x}$.

The operators in Definition 3.2 correspond directly to the components of the preconditioned system: R represents $(-\Delta + V_1)^{-1}$, K represents $(-\Delta + V_1)^{-1}V_2$, and K_h is the discrete version of K . We now establish their key properties.

LEMMA 3.3. *Under the setting of Definition 3.2:*

- (a) $K = R \circ (V_2 \cdot) \circ \iota$, where $\iota : H_0^1(\Omega) \hookrightarrow L^2(\Omega)$ is the natural embedding. In particular, K is compact and self-adjoint on $(H_0^1(\Omega), \langle \cdot, \cdot \rangle_A)$.
(b) $K_h u_h = \Pi_h(K u_h)$ for all $u_h \in X_h$.
(c) $K = (-\Delta + V_1)^{-1}V_2$ and $K_h = (-\Delta_h + V_{1,h})^{-1}V_{2,h}$.

Proof. (a) First, the multiplication $u \mapsto V_2 u$ is bounded on L^2 , since $V_2 \in L^\infty(\Omega)$. Second, R is a bounded operator, since it represents $(-\Delta + V_1)^{-1}$. The embedding ι is compact by the Rellich–Kondrachov theorem, so $K = R \circ (V_2 \cdot) \circ \iota$ is compact. For self-adjointness, (3.3) gives $\langle Ku, v \rangle_A = \int V_2 uv$ and $\langle Kv, u \rangle_A = \int V_2 vu$. Since $\langle \cdot, \cdot \rangle_A$ is symmetric, $\langle Ku, v \rangle_A = \langle u, Kv \rangle_A$.

(b) For any $u_h, v_h \in X_h$,

$$\langle K_h u_h, v_h \rangle_A = \int V_2 u_h v_h = \langle K u_h, v_h \rangle_A = \langle \Pi_h(K u_h), v_h \rangle_A,$$

so $K_h u_h = \Pi_h(K u_h)$ for all $u_h \in X_h$, i.e., $K_h = \Pi_h K|_{X_h}$.

(c) By definition, $\langle Ku, v \rangle_A = \int V_2 u v = (V_2 u, v)_{L^2} = \langle R(V_2 u), v \rangle_A$, so $Ku = R(V_2 u)$, i.e., $K = (-\Delta + V_1)^{-1}V_2$. Similarly, $K_h u_h$ is the unique element of X_h satisfying $\langle K_h u_h, v_h \rangle_A = \int V_2 u_h v_h$ for all $v_h \in X_h$, which is precisely $(-\Delta_h + V_{1,h})^{-1}(V_{2,h} u_h)$. \square

THEOREM 3.4 (Spectral convergence of the preconditioned operator). *For a bounded domain $\Omega \subset \mathbb{R}^d$, under Assumption I, let $T = (-\Delta + V_1)^{-1}(-\Delta + V_1 + V_2) = I + K$ and $T_h = (-\Delta_h + V_{1,h})^{-1}(-\Delta_h + V_{1,h} + V_{2,h}) = I_h + K_h$, where I_h denotes the identity on X_h , be the continuous and discrete preconditioned operators, and let $\tilde{K}_h = \Pi_h K \Pi_h : H_0^1(\Omega) \rightarrow H_0^1(\Omega)$. Then:*

- (i) **Norm convergence.** $\|\tilde{K}_h - K\| \rightarrow 0$ as $h \rightarrow 0$ in the operator norm on $(H_0^1(\Omega), \|\cdot\|_A)$.
(ii) **Spectral convergence and clustering.** For every $\epsilon > 0$, T_h has at most $M(\epsilon)$ eigenvalues outside $(1-\epsilon, 1+\epsilon)$, where $M(\epsilon)$ is independent of h . Each nonzero eigenvalue μ of K with multiplicity m is approximated by exactly m eigenvalues of K_h converging to μ as $h \rightarrow 0$.

- (iii) **Uniform condition number.** If $-\Delta + V_1 + V_2 > 0$, then $\kappa(T_h) \leq \kappa(T)$ for every h , and $\kappa(T_h) \rightarrow \kappa(T)$ as $h \rightarrow 0$.

Proof. Since Π_h maps $H_0^1(\Omega)$ onto X_h , $\tilde{K}_h = \Pi_h K \Pi_h$ maps X_h^\perp to zero and restricts to K_h on X_h (by Lemma 3.3(b), $\Pi_h K u_h = K_h u_h$ for $u_h \in X_h$). Therefore the nonzero eigenvalues of \tilde{K}_h are exactly those of K_h : if $\tilde{K}_h f = \mu f$ with $\mu \neq 0$, then $f = \mu^{-1} \tilde{K}_h f \in X_h$, so f is an eigenfunction of K_h .

Part (i): Norm convergence. Write $K - \tilde{K}_h = (I - \Pi_h)K + \Pi_h K (I - \Pi_h)$. Since K and Π_h are both self-adjoint in $\langle \cdot, \cdot \rangle_A$, the adjoint of $\Pi_h K (I - \Pi_h)$ is $(I - \Pi_h)K \Pi_h$. Because $\|B\| = \|B^*\|$ for any bounded operator B and its adjoint B^* on a Hilbert space, $\|\Pi_h K (I - \Pi_h)\| = \|(I - \Pi_h)K \Pi_h\| \leq \|(I - \Pi_h)K\| \|\Pi_h\| = \|(I - \Pi_h)K\|$, thus

$$(3.4) \quad \|\tilde{K}_h - K\| \leq 2 \|(I - \Pi_h)K\|.$$

It remains to show $\|(I - \Pi_h)K\| \rightarrow 0$. Since K is compact, the image of the closed unit ball $\bar{B}_1 = \{f \in H_0^1(\Omega) : \|f\|_A \leq 1\}$ under K is precompact in $(H_0^1(\Omega), \|\cdot\|_A)$. Consider any fixed $\epsilon > 0$, and cover $K(\bar{B}_1)$ by finitely many ϵ -balls centered at $g_1, \dots, g_M \in H_0^1(\Omega)$. Since $C_c^\infty(\Omega)$ is dense in $H_0^1(\Omega)$ and conforming finite element spaces approximate smooth functions as $h \rightarrow 0$ (by polynomial interpolation), $\bigcup_h X_h$ is dense in $H_0^1(\Omega)$, so $(I - \Pi_h)g_j \rightarrow 0$ in $\|\cdot\|_A$ for each j , thus there exists h_0 such that $\|(I - \Pi_h)g_j\|_A < \epsilon$ for all j and all $h < h_0$. For any f with $\|f\|_A \leq 1$, choose g_j with $\|Kf - g_j\|_A < \epsilon$. Since $\|I - \Pi_h\| \leq 1$ (orthogonal projection),

$$\|(I - \Pi_h)Kf\|_A \leq \underbrace{\|(I - \Pi_h)(Kf - g_j)\|_A}_{\leq \epsilon} + \underbrace{\|(I - \Pi_h)g_j\|_A}_{< \epsilon} < 2\epsilon.$$

Hence $\|(I - \Pi_h)K\| \leq 2\epsilon$ for $h < h_0$. Since ϵ was arbitrary, $\|(I - \Pi_h)K\| \rightarrow 0$, and by (3.4), $\|\tilde{K}_h - K\| \rightarrow 0$.

Part (ii): Clustering. Since Π_h is an orthogonal projection in $\langle \cdot, \cdot \rangle_A$, its operator norm is $\|\Pi_h\| = 1$, so the singular values s_n satisfy $s_n(\tilde{K}_h) = s_n(\Pi_h K \Pi_h) \leq s_n(K)$. For self-adjoint operators, singular values s equal absolute values of eigenvalues μ , so $|\mu_n(\tilde{K}_h)| \leq |\mu_n(K)|$ for each n , where eigenvalues are ordered by decreasing absolute value. Since K is compact and self-adjoint, its eigenvalues accumulate only at 0 [31, Theorem VI.16], so for every $\epsilon > 0$, at most $M(\epsilon) < \infty$ of them satisfy $|\mu_n(K)| \geq \epsilon$. Since $|\mu_n(\tilde{K}_h)| \leq |\mu_n(K)|$, the same bound holds for \tilde{K}_h , independently of h . Hence $T_h = I_h + \tilde{K}_h$ has at most $M(\epsilon)$ eigenvalues outside $(1-\epsilon, 1+\epsilon)$.

Convergence. Since $\tilde{K}_h \rightarrow K$ in operator norm and K and \tilde{K}_h are compact and self-adjoint, Osborn's spectral approximation theory [30] applies directly. By the spectral convergence results in [30, Section 3], for each nonzero eigenvalue μ of K with multiplicity m , there exist exactly m eigenvalues of \tilde{K}_h converging to μ . Since the nonzero eigenvalues of \tilde{K}_h are exactly those of K_h , the same convergence holds for the eigenvalues of K_h .

Part (iii): Uniform condition number. For any $u_h \in X_h$ with $\|u_h\|_A = 1$,

$$\langle K_h u_h, u_h \rangle_A = \int_{\Omega} V_2 |u_h|^2 \, d\mathbf{x} = \langle K u_h, u_h \rangle_A,$$

since $u_h \in X_h \subset H_0^1(\Omega)$. By the Courant–Fischer min-max principle, $\mu_{\max}(K_h) = \max_{u_h \in X_h, \|u_h\|_A=1} \langle K u_h, u_h \rangle_A$ and $\mu_{\max}(K) = \sup_{u \in H_0^1, \|u\|_A=1} \langle K u, u \rangle_A$. Since $X_h \subset$

$H_0^1(\Omega)$, the maximum over the smaller set X_h cannot exceed the supremum over $H_0^1(\Omega)$. The same reasoning applies to μ_{\min} . Therefore:

$$\mu_{\min}(K) \leq \mu_{\min}(K_h) \quad \text{and} \quad \mu_{\max}(K_h) \leq \mu_{\max}(K).$$

Since $T_h = I_h + K_h$ and $T = I + K$, this gives $\mu_{\min}(T) \leq \mu_{\min}(T_h)$ and $\mu_{\max}(T_h) \leq \mu_{\max}(T)$. If $T > 0$, then $\mu_{\min}(T) > 0$, so

$$\kappa(T_h) = \frac{\mu_{\max}(T_h)}{\mu_{\min}(T_h)} \leq \frac{\mu_{\max}(T)}{\mu_{\min}(T)} = \kappa(T) \quad \text{for every } h.$$

Since $\mu_{\max}(K)$ and $\mu_{\min}(K)$ (if nonzero) are isolated eigenvalues of K , Part (ii) gives eigenvalues of K_h converging to them. Combined with $\mu_{\max}(K_h) \leq \mu_{\max}(K)$, this gives $\mu_{\max}(K_h) \rightarrow \mu_{\max}(K)$. Similarly $\mu_{\min}(K_h) \rightarrow \mu_{\min}(K)$. Hence $\kappa(T_h) \rightarrow \kappa(T)$. \square

THEOREM 3.5 (Domain-independent clustering for confining potentials). *Under Assumption II, consider the family of domains $\Omega_L = [-L, L]^d$ with conforming finite element subspaces $X_h \subset H_0^1(\Omega_L)$, and the preconditioned operator $T_{h,L}$ defined as in Lemma 3.3, then for every $\epsilon > 0$, there exist at most $M(\epsilon)$ eigenvalues of $T_{h,L}$ outside $(1-\epsilon, 1+\epsilon)$, where $M(\epsilon) < \infty$ is independent of both h and L . Moreover, if $-\Delta + V_1 + V_2 > 0$ on \mathbb{R}^d , then $\kappa(T_{h,L})$ is bounded independently of both h and L .*

Proof. Since V_1 is confining, the Schrödinger operator $-\Delta + V_1$ on \mathbb{R}^d has compact resolvent and therefore purely discrete spectrum $\Lambda_1 \leq \Lambda_2 \leq \dots \rightarrow \infty$ [32, Theorem XIII.16]. By the min-max principle, the n -th eigenvalue of $-\Delta + V_1$ on Ω_L satisfies

$$\lambda_n(-\Delta_L + V_1) = \min_{\substack{\dim S=n \\ S \subset H_0^1(\Omega_L)}} \max_{u \in S, \|u\|_{L^2}=1} \|u\|_A^2.$$

Restricting to $H_0^1(\Omega_L) \subset H^1(\mathbb{R}^d)$ reduces the set of candidate subspaces for the outer min, so the eigenvalues can only increase: $\lambda_n(-\Delta_L + V_1) \geq \Lambda_n$ for all n and L . The operator norm of the mapping $(-\Delta_L + V_1)^{-1} : L^2(\Omega_L) \rightarrow L^2(\Omega_L)$ satisfies

$$(3.5) \quad \|(-\Delta_L + V_1)^{-1}\|_{L^2 \rightarrow L^2} = \frac{1}{\lambda_1(-\Delta_L + V_1)} \leq \frac{1}{\Lambda_1}, \quad \text{independently of } L.$$

By contrast, for $\Omega_L = [-L, L]^d$, $\|(-\Delta_L)^{-1}\|_{L^2 \rightarrow L^2} = 1/\lambda_1(-\Delta_L) \sim L^2/\pi^2 \rightarrow \infty$.

Recall that Lemma 3.3 gives $K_L = R \circ (V_2 \cdot) \circ \iota$, where $V_2 \cdot$ is bounded with norm $\|V_2\|_{L^\infty}$. By the definition of R with test function Rf , $\|Rf\|_A^2 = (f, Rf)_{L^2} \leq \|f\|_{L^2} \|Rf\|_{L^2} \leq \|f\|_{L^2} \cdot \Lambda_1^{-1} \|f\|_{L^2}$ by (3.5), so $\|Rf\|_A \leq \Lambda_1^{-1/2} \|f\|_{L^2}$. Thus R is bounded as a map $L^2(\Omega_L) \rightarrow (H_0^1(\Omega_L), \|\cdot\|_A)$ with norm $\leq 1/\sqrt{\Lambda_1}$.

The singular values of the compact embedding $\iota : (H_0^1(\Omega_L), \|\cdot\|_A) \hookrightarrow L^2(\Omega_L)$ are determined as follows. The adjoint $\iota^* : L^2(\Omega_L) \rightarrow H_0^1(\Omega_L)$ satisfies $\langle \iota^* f, v \rangle_A = (f, v)_{L^2}$ for all $v \in H_0^1(\Omega_L)$, so $\iota^* f$ solves $(-\Delta + V_1)w = f$ weakly, i.e., $\iota^* = (-\Delta_L + V_1)^{-1}$ as a map $L^2 \rightarrow H_0^1$. Therefore $\iota^* \iota : H_0^1 \rightarrow H_0^1$ has eigenvalues $1/\lambda_n(-\Delta_L + V_1)$, and the singular values of ι are $s_n(\iota) = 1/\sqrt{\lambda_n(-\Delta_L + V_1)} \leq 1/\sqrt{\Lambda_n}$. Since K_L is self-adjoint, its singular values equal the absolute values of its eigenvalues, and the multiplicative singular value inequality gives

$$|\mu_n(K_L)| \leq \frac{\|V_2\|_{L^\infty(\mathbb{R}^d)}}{\sqrt{\Lambda_1 \Lambda_n}}.$$

Therefore $|\mu_n(K_L)| \geq \epsilon$ requires $\Lambda_n \leq \|V_2\|_{L^\infty}^2 / (\Lambda_1 \epsilon^2)$, which holds for at most $M(\epsilon)$ values of n , independently of L . This bound transfers to the discrete operators.

Define $\tilde{K}_{h,L} = \Pi_h K_L \Pi_h$ as in Theorem 3.4. Since $\|\Pi_h\| = 1$ (orthogonal projection), the singular value submultiplicativity gives $s_n(\Pi_h K_L \Pi_h) \leq s_n(K_L)$. For self-adjoint operators $|\mu_n| = s_n$, so $|\mu_n(K_{h,L})| \leq |\mu_n(K_L)|$ for each n . Hence $K_{h,L}$ also has at most $M(\epsilon)$ eigenvalues outside $[-\epsilon, \epsilon]$, independently of both h and L .

For the condition number bound, Theorem 3.4(iii) gives $\kappa(T_{h,L}) \leq \kappa(T_L)$ for each L . It remains to show $\kappa(T_L)$ is bounded independently of L . Let $K_{\mathbb{R}^d} = (-\Delta + V_1)^{-1} V_2$ on \mathbb{R}^d (well-defined since V_1 is confining). Any $u \in H_0^1(\Omega_L)$, extended by zero to $\tilde{u} \in H^1(\mathbb{R}^d)$, satisfies $\|\tilde{u}\|_A = \|u\|_A$ and $\langle K_{\mathbb{R}^d} \tilde{u}, \tilde{u} \rangle_A = \int V_2 |\tilde{u}|^2 = \int_{\Omega_L} V_2 |u|^2 = \langle K_L u, u \rangle_A$. Thus the Rayleigh quotients of K_L over $H_0^1(\Omega_L)$ are a subset of those of $K_{\mathbb{R}^d}$ over $H^1(\mathbb{R}^d)$, giving $\mu_{\min}(K_L) \geq \mu_{\min}(K_{\mathbb{R}^d})$ and $\mu_{\max}(K_L) \leq \mu_{\max}(K_{\mathbb{R}^d})$. Therefore $\kappa(T_L) \leq \kappa(T_{\mathbb{R}^d})$ for all L , and $\kappa(T_{h,L}) \leq \kappa(T_{\mathbb{R}^d})$ for all h and L . \square

REMARK 3.6 (Grid-independent PCG convergence). *For the stirrer potential (3.2), V_1 is confining and $V_2 \in L^\infty(\mathbb{R}^d)$, so Theorem 3.5 guarantees that the eigenvalues of $T_{h,L}$ cluster near 1 with at most $M(\epsilon)$ outliers, and $\kappa(T_{h,L})$ is bounded, independently of both h and L , which explains mesh- and domain-independent PCG iteration counts. In particular, CG effectively ignores finitely many outlier eigenvalues [37], which can explain the fast convergence (5–6 iterations) observed in Example 3.1 (Figure 1, bottom right), as well as the 5 iterations on \mathbb{R}^3 with the Hermite spectral method (Figure 9 in Appendix A). For the quartic potential (3.1), $V_2 \notin L^\infty(\mathbb{R}^d)$, so only Theorem 3.4 applies. For each fixed L , $\kappa(T_h) \leq \kappa(T)$ ensures mesh-independent iteration counts (Figure 1, top left), but $\kappa(T_L)$ grows with L , and iterations increase as L increases (Figure 1, bottom left).*

4. Ground State Computation.

4.1. Linear ground state via shifted inverse iteration. When $V = V_1$ is fully separable, the tensor-product solver computes $(-\Delta + V_1)^{-1} b$ directly, which can be used in shifted inverse iteration (power method for $(-\Delta + V_1 - \sigma)^{-1}$) for computing the ground state eigenvector of $(-\Delta + V_1)u = \lambda u$. We use the potential in [9]:

$$(4.1) \quad V_1(x, y, z) = \sum_{k=1}^3 (x_k^2 + 100 \sin^2(\pi x_k/4)).$$

TABLE 2

Shifted inverse iteration for the ground state of $(-\Delta + V_1)u = \lambda u$ on $[-8, 8]^3$, Q^{10} SEM, FP64. Potential (4.1). Shift $\sigma = 0.9 \lambda_{\min}(-\Delta + V_1)$. Convergence criterion $|\Delta \lambda|/|\lambda| < 10^{-12}$. Ground state eigenvalue $\lambda_1 = 23.2878438176$.

GPU	DoFs	Setup (s)	JIT (s) [†]	Iters / time (s)	Peak mem (GB)
A100	599 ³	6.2	1.0	9 / 1.25	11.2
A100	999 ³	6.4	4.3	9 / 7.61	52.1
GH200	999 ³	9.3	0.9	9 / 3.50	52.1
GH200	1099 ³	9.2	1.2	9 / 5.03	69.4

[†] JAX/XLA compilation time. At $n=999$: GH200 is $2.2\times$ faster per solve than A100 (0.39s vs. 0.85s). 1.33×10^9 DoFs converge in 5s of iteration time on a single GH200.

Table 2 shows that the shifted inverse iteration converges in 9 iterations regardless of grid size, producing the ground state of $(-\Delta + V_1)u = \lambda u$. This eigenfunction will serve as a natural initial guess for the nonlinear GPE gradient flow below.

4.2. GPE ground state via Sobolev gradient flow. We consider the ground state of the defocusing ($\beta > 0$) Gross–Pitaevskii eigenvalue problem

$$(4.2) \quad -\Delta u + V(\mathbf{x})u + \beta |u|^2 u = \lambda u, \quad \mathbf{x} \in \Omega \subset \mathbb{R}^3, \quad \|u\|_{L^2} = 1,$$

with potential $V \geq 0$ and the parameter $\beta > 0$. The ground state minimizes

$$(4.3) \quad E(u) = \frac{1}{2} \int_{\Omega} (|\nabla u|^2 + V|u|^2) d\mathbf{x} + \frac{\beta}{4} \int_{\Omega} |u|^4 d\mathbf{x}.$$

For $\beta > 0$, E has a unique positive ground state [20, 9], thus all computations in this section use real arithmetic. The ground state can be computed by the normalized gradient flow (GFDN) [4] or by projected Sobolev gradient flows [20, 11, 9].

4.3. Riemannian gradient flows. The Sobolev gradient flows can also be perceived as Riemannian gradient descent methods. We consider two Riemannian gradient flows on the L^2 unit sphere $\mathcal{S} = \{u : \|u\|_{L^2} = 1\}$. Both take the form

$$(4.4) \quad u^{n+1} = \frac{u^n - \tau \nabla_g^{\mathcal{R}} E(u^n)}{\|u^n - \tau \nabla_g^{\mathcal{R}} E(u^n)\|_{L^2}},$$

where $\nabla_g^{\mathcal{R}} E$ is the Riemannian gradient with respect to the metric g , and $\tau > 0$ is the step size. They differ only in the choice of g . We consider just two of them.

Modified H^1 flow [9]. The metric is

$$(4.5) \quad g_{H^1}(w, z) = (\nabla w, \nabla z) + \alpha(w, z), \quad \alpha > 0.$$

Each iteration requires solving $(-\Delta + \alpha I)w = (-\Delta + V + \beta u^2)u$ and a projection step, amounting to two direct solves of $(-\Delta + \alpha I)^{-1}$ per iteration, a separable tensor-product operation at cost $O(N^{4/3})$ in 3D.

a_u flow [20]. The metric depends on the current iterate u :

$$(4.6) \quad g_{a_u}(w, z) = (\nabla w, \nabla z) + (w, Vz) + \beta(w, u^2 z).$$

Each iteration requires solving $(-\Delta + V + \beta u^2)^{-1}$. We solve this by PCG with preconditioner $(-\Delta + V)^{-1}$, which is a separable tensor-product solve. We refer to [20, 9] for more details about a_u flow. The a_u metric adapts to the current iterate. It reduces the iteration count, but each step is more expensive because of the PCG solve. The tensor-product solver enters both methods: (i) shifted inverse iteration provides the eigenfunction of the linearized problem $(-\Delta + V_1)u = \lambda u$ as an initial guess (Section 4.1), (ii) the modified H^1 flow requires $(-\Delta + \alpha I)^{-1}$ (direct solve), and (iii) the a_u flow uses $(-\Delta + V)^{-1}$ as a PCG preconditioner.

4.4. Numerical results. When FP32 is used below for the PCG solves in the a_u flow, the offline eigendecompositions per axis are still computed in FP64. We consider the ground state of (4.2) for a potential $V = V_1$ with V_1 given in (4.1).

EXAMPLE 4.1 (GPE ground state with eigenfunction initial guess). *Since the GPE ground state approaches the linear ground state as $\beta \rightarrow 0$, the eigenfunction from Table 2 provides a good initial guess for moderate β . Table 3 compares the modified H^1 flow [9] with two initial guesses: a constant function $u_0 \equiv c$ (normalized s.t. $\|u_0\|_{L^2} = 1$) and the linear ground state from shifted inverse iteration. Both use Q^{20} SEM with 599^3 DoFs, $\alpha = 20$, $\tau = 0.1$, tested for $\beta = 10$ and 100 on an NVIDIA*

GH200 96 GB GPU. For moderate β , the nonlinear ground state remains close to the linear eigenfunction, so the eigenfunction initial guess starts the flow near the solution. Figure 2 illustrates the progression: at $\beta = 100$ the lattice structure is already emerging but the solution remains concentrated near the center, while at $\beta = 1600$ the ground state has spread into a broad profile far from the linear eigenfunction. As shown in Table 3, for $\beta = 10, 100$, modified H^1 flow with both initializations converges to the same energy and eigenvalue, and the eigenfunction initial guess saves 35–71% of total time with 39–77% fewer iterations. Figure 3 illustrates that both H^1 flow and a_u flow for $\beta = 100$ can benefit from the eigenfunction initial guess. But for $\beta = 1600$, as shown in Table 4 ($N = 599^3$) and Figure 4 ($N = 999^3$), the eigenfunction is no longer a good initial guess. Both Figure 3 and Figure 4 also show that a_u flow can be efficiently implemented by the PCG with the proposed preconditioner $(-\Delta + V_1)^{-1}$.

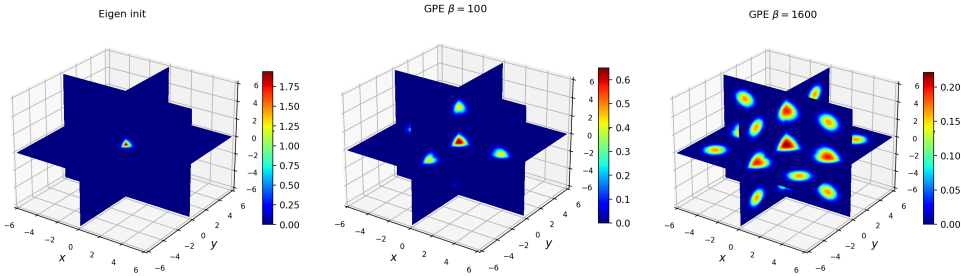


FIG. 2. Cross-sections of u at $x=0, y=0, z=0$, plotted on $[-6, 6]^3$. Q^{20} SEM, 199^3 DoFs, computed on $[-8, 8]^3$. Each panel uses its own color scale. Left: eigenfunction initial guess (linear ground state, $\beta=0$). Center: GPE ground state, $\beta=100$. Right: GPE ground state, $\beta=1600$.

TABLE 3

Modified H^1 flow for the GPE ground state on $[-8, 8]^3$, Q^{20} SEM, FP64, $\alpha = 20$, step size $\tau = 0.1$, 599^3 DoFs, GH200. Potential (4.1). Convergence criterion: $|E_k - E^*|/|E^*| < 10^{-14}$. The total computation time includes both off-line and iteration time.

β	Init	H^1 iters	Total (s)	Energy	Eigenvalue
10	constant	745	122.0	14.1965761916	32.4916917439
	eigenfunction	175	34.8	14.1965761916	32.4916917439
100	constant	660	111.4	20.6824463703	47.7831207152
	eigenfunction	405	71.9	20.6824463703	47.7831207152

TABLE 4

Comparison of a_u flow and modified H^1 flow for $\beta = 1600$, Q^{20} SEM, $599^3 \approx 2.1 \times 10^8$ DoFs, FP64, $\alpha=20$, step size $\tau=0.1$ for modified H^1 and $\tau=1$ for a_u , GH200.

Method	Initialization	Iters	Linear solves	Time (s)	Energy
a_u flow	constant	66	790	72.8	33.80227900550
a_u flow	eigenfunction	147	1846	171.9	33.80227900550
Modified H^1	constant	272	544	42.6	33.80227900551
Modified H^1	eigenfunction	not converging			

Convergence criterion: $|E_k - E^*|/|E^*| < 10^{-12}$, where $E^* = 33.80227900547423$.

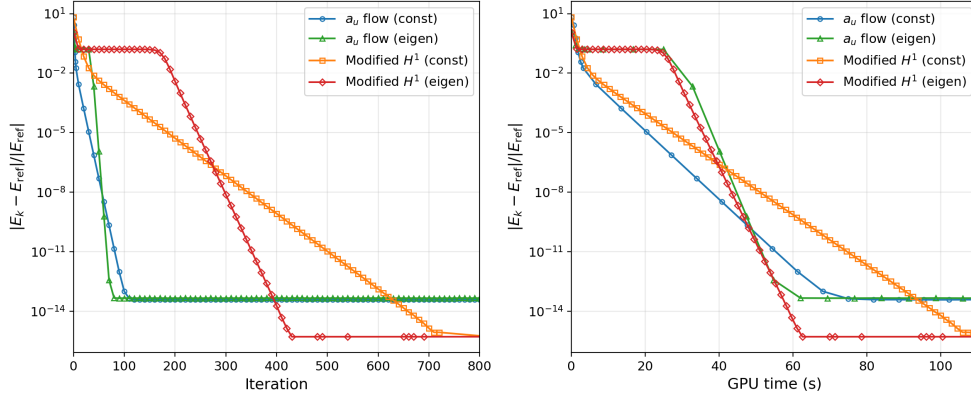


FIG. 3. Comparison of a_u flow and modified H^1 flow for $\beta = 100$, Q^{20} SEM, $599^3 \approx 2.1 \times 10^8$ DoFs, GH200. Left: relative energy error vs. iteration. Right: relative energy error vs. GPU time.

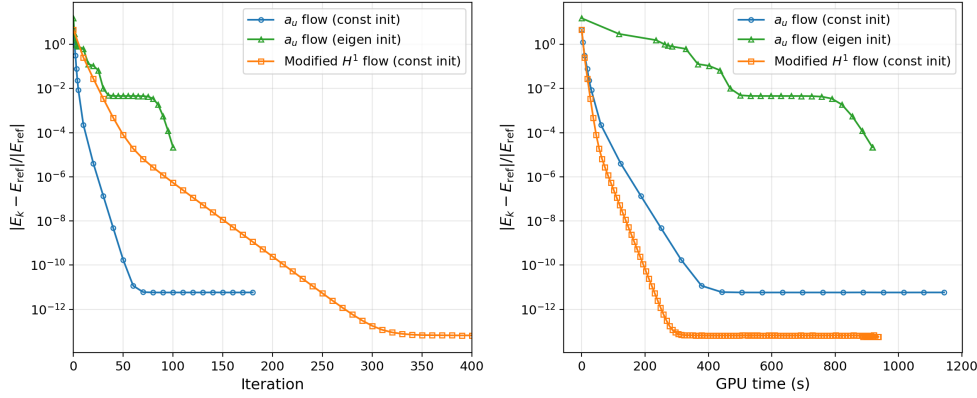


FIG. 4. Comparison of a_u flow and modified H^1 flow for $\beta = 1600$, Q^{20} SEM, $999^3 \approx 9.9 \times 10^8$ DoFs, constant initial guess, GH200. Left: relative energy error vs. iteration. Right: relative energy error vs. GPU time. The reference energy $E^* = 33.80227900547$ is from [9].

5. Hamiltonian Simulation in 3D. We consider the Schrödinger equation

$$(5.1) \quad i \partial_t \psi = H \psi, \quad H = -\Delta + V, \quad \psi(\cdot, 0) = \psi_0,$$

on $\Omega \subset \mathbb{R}^3$ with either periodic or Dirichlet boundary conditions. When V is separable, the tensor-product solver gives the exact propagator $e^{-iH\Delta t}$. When V is non-separable, it provides the propagator for each operator-splitting sub-step.

5.1. Splitting methods and classical implementation. We split $H = A + B$ with $A = -\Delta$ (kinetic) and $B = V$ (potential). The standard Strang splitting $e^{-iA\Delta t/2} e^{-iB\Delta t} e^{-iA\Delta t/2}$ is second-order in Δt , but its operator-norm error grows with the spectral radius of $[A, B]$, which may scale with N . Two recent quantum algorithms consider the interaction-picture Hamiltonian $H_I(s) = e^{iAs} B e^{-iAs}$ and apply the Magnus expansion to the time-ordered evolution:

- The $qHOP$ algorithm [1] uses the first-order Magnus truncation, achieving

$O(\Delta t^2)$ with an error constant independent of N .

- The *Magnus-2* algorithm [12] adds a commutator correction (second-order Magnus), achieving $O(\Delta t^4)$ superconvergence [7, 14].

Both methods require a matrix exponential of a sum of interaction-picture Hamiltonians, which on a quantum computer is implemented via LCU [1]. Classically, e^{iAs} is computed by the tensor-product propagator and $e^{-iB\Delta t}$ is pointwise, so each factor $\exp(-i w_k \Delta t H_I(s_k))$ can be evaluated exactly:

$$e^{-i w_k \Delta t H_I(s_k)} = e^{iAs_k} e^{-i w_k \Delta t B} e^{-iAs_k},$$

which leads to two families of methods, implemented via tensor-product propagations.

$O(\Delta t^2)$ approximated qHOP via product formula. The qHOP approximation [1] replaces the time-ordered exponential by the first-order Magnus truncation in the interaction picture (see [12, Eq. (2)]):

$$e^{-iH\Delta t} = e^{-iA\Delta t} \mathcal{T} \exp\left(-i \int_0^{\Delta t} H_I(s) ds\right) \approx e^{-iA\Delta t} \exp\left(-i \Delta t \sum_{k=1}^M w_k H_I(s_k)\right),$$

where $s_k \in [0, \Delta t]$ are Gauss–Legendre nodes and w_k ($\sum_{k=1}^M w_k = 1$) are the corresponding normalized Gauss–Legendre weights. We implement this classically via the product approximation

$$(5.2) \quad \exp\left(-i \Delta t \sum_{k=1}^M w_k H_I(s_k)\right) \approx \prod_{k=1}^M e^{-i w_k \Delta t H_I(s_k)}.$$

Since $H_I(s_k) = e^{iAs_k} B e^{-iAs_k}$, each factor in the product is computed *exactly* as $e^{-i w_k \Delta t H_I(s_k)} = e^{iAs_k} e^{-i w_k \Delta t B} e^{-iAs_k}$ (two tensor-product propagations plus one pointwise multiplication). Combining (5.2) with $e^{-iH\Delta t} = e^{-iA\Delta t} \mathcal{T} \exp(\dots)$ gives the full time step $e^{-iH\Delta t} \approx e^{-iA\Delta t} \prod_{k=1}^M e^{-i w_k \Delta t H_I(s_k)}$, where the approximation comes from the quadrature and product formula (5.2).

REMARK 5.1 (Order of the product formula). *The product formula (5.2) replaces $\exp(\text{sum})$ by a product of exponentials, which is in general a first-order Lie–Trotter approximation with error governed by the commutators $[A_j, A_k]$ where $A_k = -i w_k \Delta t H_I(s_k)$. In Lie–Trotter splitting of two different operators A and B , the commutator $[A, B]$ is a fixed operator, giving first-order global error $O(\Delta t)$. Here, however, all the operators $H_I(s_k)$ have $s_k \in [0, \Delta t]$, so as $\Delta t \rightarrow 0$, $H_I(s_k) \rightarrow H_I(0) = B$ for all k , and the commutators $[H_I(s_j), H_I(s_k)] \rightarrow [B, B] = 0$. More precisely, smoothness of $H_I(s)$ in s gives $[H_I(s_j), H_I(s_k)] = O(|s_j - s_k|) = O(\Delta t)$, so each $[A_j, A_k] = w_j w_k \Delta t^2 [H_I(s_j), H_I(s_k)] = O(\Delta t^3)$. The product formula error is therefore $O(\Delta t^3)$ per step and $O(\Delta t^2)$ globally, matching the qHOP approximation order.*

$O(\Delta t^4)$ approximated Magnus-2 via Yoshida composition. The Magnus-2 algorithm [12] replaces the first-order Magnus truncation with the second-order one:

$$e^{-iH\Delta t} \approx e^{-iA\Delta t} \exp(\Omega_1 + \Omega_2),$$

where $\Omega_1 = -i \Delta t \sum_{k=1}^M w_k H_I(s_k)$ is the qHOP exponent and

$$\Omega_2 = -\frac{1}{2} \int_0^{\Delta t} \int_0^{s_1} [H_I(s_1), H_I(s_2)] ds_2 ds_1$$

is the commutator correction, achieving $O(\Delta t^4)$ superconvergence. On a quantum computer, $e^{\Omega_1 + \Omega_2}$ is implemented via LCU. Classically, it is impractical to compute $e^{\Omega_1 + \Omega_2}$ directly. Instead, we apply the fourth-order Yoshida splitting [38] to the approximated qHOP:

$$(5.3) \quad e^{-iH\Delta t} \approx P(\gamma_1 \Delta t) P(\gamma_2 \Delta t) P(\gamma_1 \Delta t), \quad \gamma_1 = \frac{1}{2 - 2^{1/3}}, \quad \gamma_2 = \frac{-2^{1/3}}{2 - 2^{1/3}},$$

where $P(h)$ denotes one approximated qHOP step with step size h , i.e., $P(h) = e^{-iAh} \prod_{k=1}^M e^{-i w_k h H_I(s_k)}$, and $\gamma_1 + \gamma_2 + \gamma_1 = 1$. Yoshida cancels the $O(h^3)$ leading error ($2\gamma_1^3 + \gamma_2^3 = 0$), yielding $O(\Delta t^4)$ global accuracy, the same order as the original Magnus-2 method. Although (5.3) is derived by applying Yoshida composition to the approximated qHOP rather than by directly approximating $e^{\Omega_1 + \Omega_2}$, it achieves the same $O(\Delta t^4)$ rate as the original Magnus-2, and can therefore be regarded as an approximation to Magnus-2.

REMARK 5.2 (Classical splitting as limiting cases). *qHOP with $M=1$ (midpoint rule) recovers the Strang splitting [1]. At the next order, our approximated Magnus-2 with $M=1$ reduces to the plain Yoshida method. Thus Strang and Yoshida can be perceived as the $M=1$ special cases of such approximated versions of qHOP and Magnus-2, respectively, while larger M reduces the error constant.*

REMARK 5.3 (Cost per step). *For $M \geq 2$, the approximated qHOP in (5.2) has a direct count of $(2M+1)$ tensor-product propagations per step, i.e., number of multiplying $e^{\pm iAs_k}$ per step. For $M = 1$, the optimized Strang form $e^{-iV\Delta t/2} e^{-iA\Delta t} e^{-iV\Delta t/2}$ needs only 1 tensor-product propagation per step. A better implementation for $M > 1$ is to merge two adjacent factors, e.g., for $M = 3$, the merged form of the qHOP is*

$$e^{-iA(\Delta t - s_3)} e^{-iw_3 \Delta t B} e^{-iA(s_3 - s_2)} e^{-iw_2 \Delta t B} e^{-iA(s_2 - s_1)} e^{-iw_1 \Delta t B} e^{-iAs_1},$$

which has only $(M+1)$ A -propagations per step. By merging e^{-iAs_1} at step n with $e^{-iA(\Delta t - s_M)}$ at step $n+1$, the cost would be M A -propagations per time step. Applying the same merging strategy to each of the three Yoshida sub-steps and across consecutive time steps, the approximated Magnus-2 costs $3M$ A -propagations per step asymptotically for $M \geq 2$, and 3 A -propagations plus 3 pointwise B -multiplications per step for $M = 1$ (plain Yoshida).

5.2. Exact propagator as reference for testing splitting methods. When $V = V_1$ is separable, the eigendecomposition $H = T \Lambda T^{-1}$ gives the exact propagator

$$(5.4) \quad e^{-iH\Delta t} \psi = T (e^{-i\Lambda\Delta t} \odot (T^{-1} \psi)),$$

at cost $O(N^{4/3})$ in 3D. We test with the separable potential (4.1) from Section 4.1 on $[-8, 8]^3$, Dirichlet BC, Q^k SEM, and the exact propagator (5.4) as reference.

Most existing numerical tests of these methods are in 1D with $N \leq 1024$, using dense matrix exponentials (`expm`). Our tensor-product solver provides the exact propagator as a reference solution at $\sim 10^8$ DoFs, enabling large-scale 3D validation of the splitting convergence rates. In the rest of this section, “qHOP” and “Magnus-2” refer to the approximated versions implemented via the product formula (5.2) and Yoshida composition (5.3), respectively.

EXAMPLE 5.1 (Order of approximated qHOP). *Table 5 reports qHOP with $M = 1$ (Strang), 3, 5, and 7 on a GH200 GPU. The discretization uses Q^{10} SEM with 499^3 DoFs, complex128 arithmetic, and $T = 0.1$. The initial condition is $\psi_0(\mathbf{x}) =$*

$\prod_{k=1}^3 \sin(\pi(x_k+L)/2L)$. The observed convergence is $O(\Delta t^2)$ for all M . Relative to Strang, the error constant is smaller by ~ 5 ($M=3$), ~ 13 ($M=5$), and ~ 24 ($M=7$). See Remark 5.3 for cost comparison.

TABLE 5
 $qHOP$ splitting error $\|\psi_{\text{split}}(T) - \psi_{\text{exact}}(T)\|_2$ on GH200, Q^{10} SEM, 499³ DoFs, complex128, $T=0.1$. $M=1$ is the Strang splitting. t (s) is the GPU time.

Δt	$M = 1$ (Strang)			$M = 3$			$M = 5$			$M = 7$		
	Error	Rate	t (s)	Error	Rate	t (s)	Error	Rate	t (s)	Error	Rate	t (s)
0.1	5.85e-1	–	0.1	1.07e-1	–	0.4	4.25e-2	–	0.5	2.28e-2	–	0.7
0.01	5.22e-3	2.05	0.9	1.02e-3	2.02	3.0	4.11e-4	2.01	4.8	2.21e-4	2.01	6.7
0.005	1.30e-3	2.01	1.9	2.55e-4	2.00	5.8	1.03e-4	2.00	9.6	5.52e-5	2.00	13
0.001	5.21e-5	2.00	9.5	1.02e-5	2.00	29	4.11e-6	2.00	48	2.21e-6	2.00	67

5.3. Non-separable potential: manufactured exact solution. When $V = V_1 + V_2$ is not fully separable, we use the PCG solver from Section 3.2 to compute the ground state (λ_1, u_1) of $H = -\Delta + V_1 + V_2$. The function

$$(5.5) \quad \psi_{\text{exact}}(\mathbf{x}, t) = e^{-i\lambda_1 t} u_1(\mathbf{x})$$

is a stationary solution of (5.1), against which we verify splitting convergence orders. We test with the stirrer potential (3.2) on $[-8, 8]^3$, Dirichlet BC, Q^{20} SEM, and we also consider splitting $H = A + B$ with $A = -\Delta + V_1$ and $B = V_2$.

5.3.1. Multi-level generation of the reference solution. The ground state (λ_1, u_1) of $H = A + B$ is computed by shifted inverse iteration: each step solves $(H - \sigma I)w = u$ via PCG with the tensor-product preconditioner $A^{-1} = (-\Delta + V_1)^{-1}$ from Section 3.2. The shift $\sigma = 0.9 \lambda_{\min}(A)$ keeps $H - \sigma I$ positive definite (since $V_2 \geq 0$) and close enough to λ_1 for rapid convergence. The initial guess is the ground state eigenfunction of A , obtained from the tensor-product eigendecomposition.

To efficiently reach large grid sizes, we use a multi-level strategy: solve on a coarse grid, interpolate the eigenvector to the next finer grid via tensor-product linear interpolation, and continue the inverse iteration. Each refinement inherits a good initial guess, reducing both the number of inverse iterations and the PCG iterations per step. Table 6 demonstrates this for the stirrer potential (3.2) on an A100 GPU. At the finest level (499³ DoFs), only 11 inverse iterations with 21 PCG iterations each are needed, a total of 231 applications of $(-\Delta + V_1)^{-1}$. The entire multi-level computation takes about one minute, producing a ground state accurate to $|\Delta\lambda|/|\lambda| < 10^{-13}$.

TABLE 6
Multi-level shifted inverse iteration for the ground state of $H = -\Delta + V_1 + V_2$, stirrer potential (3.2), Q^{20} SEM, FP64, A100. Preconditioner: $(-\Delta + V_1)^{-1}$, PCG tolerance 10^{-12} , shift $\sigma = 0.9 \lambda_{\min}(A)$. Ground state eigenvalue $\lambda_1 = 5.286155366963$.

n (DoFs)	Setup (s)	Interpolation (s)	Inverse iters	PCG/iter	Total A^{-1}
99 ³	6.1	—	30	75	2242
199 ³	2.6	0.3	21	24	504
499 ³	2.6	0.5	11	21	231

Initial guess at 99³: ground state of $A = -\Delta + V_1$. **Total wall time: ~ 62 s on A100.**

5.3.2. Testing splitting methods for Hamiltonian simulations.

EXAMPLE 5.2 (Order of approximated qHOP for non-separable stirrer potential).

We test qHOP with $M = 1$ (Strang), 3, 5, and 7, 499^3 DoFs, complex128, $T = 0.1$, on a GH200 GPU. The initial condition is $\psi_0 = u_1$ (ground state eigenvector, $\lambda_1 = 5.286155366963$). Table 7 compares two splittings: $A = -\Delta$, $B = V_1 + V_2$ (top half), and $A = -\Delta + V_1$, $B = V_2$ (bottom half), where A includes the separable part of the potential. Both show $O(\Delta t^2)$ convergence for all M , but the splitting $A = -\Delta + V_1$ gives $\sim 1.5\text{--}3\times$ smaller errors because $\|V_2\| \ll \|V_1 + V_2\|$. For qHOP as a quantum algorithm, $A = -\Delta$ is required since A must be the operator that can be fast-forwarded on a quantum computer. For classical ODE/PDE solvers, including the separable potential in A is advantageous.

TABLE 7

qHOP splitting error for the non-separable stirrer potential (3.2), Q^{20} SEM, 499^3 DoFs, complex128, $T=0.1$, GH200. t (s) is the GPU time. Reference: manufactured solution (5.5).

Δt	$M = 1$ (Strang)			$M = 3$			$M = 5$			$M = 7$		
	Error	Rate	t (s)	Error	Rate	t (s)	Error	Rate	t (s)	Error	Rate	t (s)
<i>Splitting $A = -\Delta$, $B = V_1 + V_2$</i>												
0.1	8.04e-3	–	0.7	3.93e-4	–	1.0	1.58e-4	–	1.1	8.49e-5	–	1.4
0.01	7.73e-5	2.02	1.6	3.90e-6	2.00	3.5	1.57e-6	2.00	5.6	8.44e-7	2.00	7.8
0.005	1.93e-5	2.00	2.6	9.74e-7	2.00	6.5	3.93e-7	2.00	11	2.11e-7	2.00	15
0.001	7.73e-7	2.00	11	3.94e-8	1.99	30	1.64e-8	1.97	51	9.46e-9	1.93	72
<i>Splitting $A = -\Delta + V_1$, $B = V_2$</i>												
0.1	4.75e-3	–	0.9	1.37e-4	–	1.0	5.50e-5	–	1.3	2.96e-5	–	1.5
0.01	4.52e-5	2.02	1.7	1.35e-6	2.01	3.7	5.47e-7	2.00	5.6	2.95e-7	2.00	7.7
0.005	1.13e-5	2.00	2.6	3.40e-7	1.99	6.6	1.38e-7	1.99	10	7.50e-8	1.98	15
0.001	4.52e-7	2.00	10	1.61e-8	1.90	30	8.99e-9	1.70	49	7.19e-9	1.46	71

EXAMPLE 5.3 (Order of approximated Magnus-2 for non-separable stirrer potential). We use the same setup, but with $T = 1$. Table 8 compares the two splittings as in Table 7. Both show $O(\Delta t^4)$ convergence for $M \geq 3$. The splitting $A = -\Delta + V_1$, $B = V_2$ again gives smaller errors, with the advantage growing with M .

6. Multi-Body Hamiltonian Simulation (4D, 6D, 9D). In this section we consider multi-particle systems with pairwise interactions in 4D, 6D, and 9D. As in Section 5.3, the reference solution is $\psi_{\text{exact}} = e^{-i\lambda_1 t} u_1$, with the ground state computed by PCG using $(-\Delta + V_{\text{trap}})^{-1}$ as preconditioner.

6.1. Two particles in 2D with Coulomb interaction (4D). We consider two quantum particles in a 2D harmonic trap with Coulomb interaction. The Coulomb singularity $1/|\mathbf{x}_1 - \mathbf{x}_2|$ at $\mathbf{x}_1 = \mathbf{x}_2$ needs be regularized unless special transformation is used. One approach is the cell-averaged potential of [15], which integrates $1/|\mathbf{x}_1 - \mathbf{x}_2|$ against the basis functions. We use the simpler soft Coulomb potential $c/\sqrt{|\mathbf{x}_1 - \mathbf{x}_2|^2 + \delta^2}$ with a small parameter $\delta > 0$, which is smooth for any $\delta > 0$, so we expect $O(\Delta t)$ for Lie–Trotter and $O(\Delta t^2)$ for Strang, although Lie–Trotter is only $O(\Delta t^{1/4})$ for the exact (unregularized) Coulomb potential [13]. The equation is

$$(6.1) \quad i \partial_t \psi = (-\Delta_{\mathbf{x}_1} - \Delta_{\mathbf{x}_2} + V_{\text{trap}}(\mathbf{x}_1) + V_{\text{trap}}(\mathbf{x}_2) + \frac{c}{\sqrt{|\mathbf{x}_1 - \mathbf{x}_2|^2 + \delta^2}}) \psi, \quad \mathbf{x}_1, \mathbf{x}_2 \in \mathbb{R}^2,$$

TABLE 8

Magnus-2 via Yoshida splitting error for the non-separable stirrer potential (3.2), Q^{20} SEM, 499^3 DoFs, complex128, $T=1$, GH200. t (s) is the GPU time. Top: $A = -\Delta$, $B = V_1 + V_2$. Bottom: $A = -\Delta + V_1$, $B = V_2$, which gives $\sim 1.5\text{--}3\times$ smaller errors. Reference: manufactured solution via multi-level inverse iteration.

Δt	$M = 1$ (Yoshida)			$M = 3$			$M = 5$			$M = 7$		
	Error	Rate	t (s)	Error	Rate	t (s)	Error	Rate	t (s)	Error	Rate	t (s)
<i>Splitting $A = -\Delta$, $B = V_1 + V_2$</i>												
0.2	8.63e-2	–	2.2	5.36e-3	–	5.1	4.61e-4	–	8.2	1.02e-4	–	11
0.125	1.30e-2	4.03	3.1	5.44e-4	4.87	7.7	2.93e-5	5.86	13	1.32e-5	4.35	18
0.1	5.34e-3	3.99	3.7	1.33e-4	6.31	9.5	1.10e-5	4.39	16	5.02e-6	4.33	22
0.05	3.39e-4	3.98	6.9	3.25e-6	5.35	19	6.77e-7	4.02	30	3.00e-7	4.06	44
<i>Splitting $A = -\Delta + V_1$, $B = V_2$</i>												
0.2	2.48e-2	–	2.2	5.06e-3	–	5.1	4.21e-4	–	8.1	7.04e-5	–	11
0.125	3.75e-3	4.02	3.1	5.15e-4	4.86	7.8	1.46e-5	7.15	13	7.29e-6	4.82	17
0.1	1.50e-3	4.11	3.8	1.20e-4	6.53	9.5	4.18e-6	5.60	16	2.37e-6	5.04	21
0.05	1.04e-4	3.85	6.5	8.50e-7	7.14	18	2.37e-7	4.14	30	1.29e-7	4.20	42

where $V_{\text{trap}}(\mathbf{x}) = |\mathbf{x}|^2$ is a harmonic trap.

6.1.1. Preconditioner comparison. To select the best preconditioner for PCG, we solve $(-\Delta + V_1 + V_2)u = f$ with a random right-hand side f on the 49^4 grid with $\delta = 0.01$, comparing three preconditioners in Table 9. The tensor-product preconditioner $(-\Delta + V_1)^{-1}$ converges in 24 iterations, far fewer than the combined preconditioner $P_C = (V_1 + V_2)^{-1/2}(-\Delta)^{-1}(V_1 + V_2)^{-1/2}$ (443 iterations). The variant $V_2^{-1/2}(-\Delta + V_1)^{-1}V_2^{-1/2}$ does not converge within 500 iterations. We therefore use $(-\Delta + V_1)^{-1}$ throughout.

TABLE 9

PCG iteration count for solving $(-\Delta + V_1 + V_2)u = f$ with three preconditioners. Q^{10} SEM, 49^4 DoFs, $\delta = 0.01$, FP64, A100. Tolerance 10^{-12} , max 500 iterations.

Preconditioner	Iters	Time (s)	Status
$(-\Delta + V_1)^{-1}$	24	0.5	converged
$(V_1 + V_2)^{-1/2}(-\Delta)^{-1}(V_1 + V_2)^{-1/2}$	443	2.9	converged
$V_2^{-1/2}(-\Delta + V_1)^{-1}V_2^{-1/2}$	500	3.0	stalled at 5×10^{-10}

6.1.2. Ground state computation. Table 10 shows the ground state computation cost for several values of δ , with $c = 1$, $V_{\text{trap}}(\mathbf{x}) = |\mathbf{x}|^2$, domain $[-8, 8]^2 \times [-8, 8]^2$. PCG is warm-started with the previous inverse iteration solution, which reduces iterations after the first few steps.

Figure 5 shows slices of the 4D ground state wavefunction for $\delta = 0.01$ and 0.0001, interpolated onto a fine grid via cell-by-cell Q^{10} polynomial reconstruction. As δ decreases, the Coulomb singularity sharpens: the 1D slice narrows, and the inter-particle correlation plot develops a more pronounced dip along $x_{1a} = x_{2a}$.

6.1.3. Splitting convergence. As in Section 5.2, “qHOP” and “Magnus-2” refer to the approximated versions (5.2) and (5.3). All 4D splitting tests use Q^{10} SEM, 99^4 DoFs, complex128, $T = 0.1$, GH200.

TABLE 10

Ground state of $H = -\Delta + V_{\text{trap}} + V_{\text{Coulomb}}$ via shifted inverse iteration with PCG (preconditioner $(-\Delta + V_{\text{trap}})^{-1}$, max 500 iterations, warm-started with the previous iteration's solution). Q^{10} SEM, $99^4 \approx 9.6 \times 10^7$ DoFs, GH200. Multi-level: coarse 49^4 solution interpolated as initial guess; shift $\sigma = \lambda_{\min}(-\Delta + V_{\text{trap}}) - 10^{-4} = 3.9999$. PCG tolerance 10^{-9} .

δ	V_C^{\max}	Inv. iters	PCG/iter	Total solves	Time (s)	λ_1
0.1	10	22	1–18	121	8	5.060514417326
0.01	100	24	1–32	204	12	5.221829172892
0.001	1,000	12	1–500 [†]	4,286	208	5.400105827385
0.0001	10,000	12	1–500 [†]	5,816	274	5.444872472429

[†] PCG reaches max 500 iterations only in the first few inverse iterations, which does not affect the final accuracy since PCG converges quickly in the last few inverse iterations.

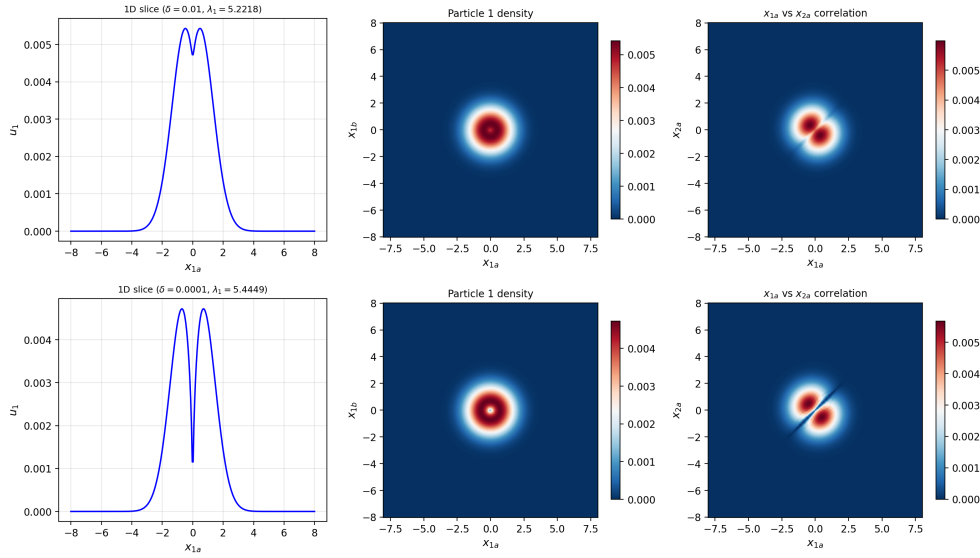


FIG. 5. Slices of the 4D Coulomb ground state for $\delta = 0.01$ (top) and $\delta = 0.0001$ (bottom), Q^{10} SEM, 99^4 DoFs. Top: 1D slice along x_{1a} . Middle: particle 1 density in the (x_{1a}, x_{1b}) plane. Bottom: x_{1a} vs. x_{2a} inter-particle correlation. The Coulomb repulsion strengthens as $\delta \rightarrow 0$. Plotted on a 300×300 fine grid via cell-by-cell Q^{10} polynomial interpolation.

EXAMPLE 6.1 (Order of approximated qHOP convergence in 4D, $\delta = 0.001$). Table 11 reports qHOP with $M = 1$ (Strang), 3, 5, 7 for the Coulomb system with $\delta = 0.001$ ($V_C^{\max} = 1000$). All methods show $O(\Delta t^2)$ convergence in the asymptotic regime ($\Delta t \leq 0.001$). Larger M reduces the error constant: at $\Delta t = 0.0005$, $M=3, 5, 7$ reduce the error by $\sim 14\times, 35\times, 65\times$ relative to Strang.

EXAMPLE 6.2 (Order of approximated Magnus-2 in 4D, $\delta = 0.1$). Table 12 shows the convergence of Magnus-2 via Yoshida with $M = 1$ (plain Yoshida), 3, 5, 7 for the Coulomb system with $\delta = 0.1$ ($V_C^{\max} = 10$). For $M = 7$, the error reaches 2.5×10^{-10} at $\Delta t = 0.001$. Larger M reduces the error constant and enters the high-order asymptotic regime at larger Δt .

TABLE 11
qHOP splitting error $\|\psi_{\text{split}}(T) - \psi_{\text{exact}}(T)\|_2$ on GH200, Q^{10} SEM, 99^4 DoFs, complex128, $T=0.1$, Coulomb $\delta = 0.001$. t (s) is the GPU time.

Δt	$M = 1$ (Strang)			$M = 3$			$M = 5$			$M = 7$		
	Error	Rate	t (s)	Error	Rate	t (s)	Error	Rate	t (s)	Error	Rate	t (s)
0.005	3.32e-1	–	1.8	4.93e-2	–	4.2	4.27e-2	–	5.9	2.96e-2	–	8.0
0.002	5.21e-2	2.02	3.3	2.51e-2	0.74	8.5	1.26e-3	3.84	13	5.18e-4	4.42	18
0.001	3.75e-2	0.47	5.9	1.33e-3	4.24	16	2.34e-4	2.43	26	1.25e-4	2.05	36
0.0005	1.98e-3	4.24	11	1.41e-4	3.24	31	5.64e-5	2.05	51	3.03e-5	2.04	71

TABLE 12
Magnus-2 via Yoshida splitting error, 99^4 DoFs, complex128, $T=0.1$, Coulomb $\delta = 0.1$. t (s) is the GPU time on GH200.

Δt	$M = 1$ (Yoshida)			$M = 3$			$M = 5$			$M = 7$		
	Error	Rate	t (s)	Error	Rate	t (s)	Error	Rate	t (s)	Error	Rate	t (s)
0.005	2.54e-3	–	3.7	7.49e-4	–	10	2.83e-4	–	16	1.51e-4	–	22
0.002	5.82e-5	4.12	8.4	2.38e-5	3.76	24	5.36e-6	4.33	39	5.52e-7	6.12	53
0.001	8.39e-6	2.79	16	1.61e-6	3.89	46	3.74e-8	7.16	77	2.54e-10	11.09	106

6.2. Two particles in 3D with Coulomb interaction (6D). We extend the 4D test to two particles in 3D ($\mathbf{x}_1, \mathbf{x}_2 \in \mathbb{R}^3$). The Hamiltonian is

$$(6.2) \quad H = -\Delta_{\mathbf{x}_1} - \Delta_{\mathbf{x}_2} + V_{\text{trap}}(\mathbf{x}_1) + V_{\text{trap}}(\mathbf{x}_2) + \frac{c}{\sqrt{|\mathbf{x}_1 - \mathbf{x}_2|^2 + \delta^2}},$$

discretized on $[-L, L]^3 \times [-L, L]^3$ with Q^{10} SEM, $29^6 \approx 5.9 \times 10^8$ DoFs. The splitting is $A = -\Delta$ (6D Laplacian), $B = V_{\text{trap}} + V_{\text{Coulomb}}$, and the reference solution is $\psi_{\text{exact}}(\mathbf{x}, t) = e^{-i\lambda_1 t} u_1(\mathbf{x})$ where (λ_1, u_1) is the ground state of H .

6.2.1. Ground state. In these TF32 runs, the offline eigendecomposition of $-\Delta + V_{\text{trap}}$ is still computed in FP64 and then cast to lower precision for PCG solves. See Table 13 for the performance. The solution is plotted in Figure 6.

TABLE 13
Ground state of the 6D Coulomb Hamiltonian (6.2), Q^{16} SEM, $N_{\text{cell}} = 2$, $n = 31$, $31^6 \approx 8.9 \times 10^8$ DoFs, TF32, $L = 5$, GH200. Shifted inverse iteration with $\sigma = 0$, PCG tolerance 10^{-4} .

δ	V_C^{max}	Inv. iters	Total PCG solves	Time (s)	λ_1
0.01	100	12	31	17	6.792689
0.001	1000	12	99	34	6.844492
0.0001	10000	12	331	94	6.861799

6.2.2. Splitting convergence.

EXAMPLE 6.3 (Order of approximated qHOP in 6D, $\delta = 0.01$). Table 14 reports qHOP with $M = 1$ (Strang), 3, 5, 7 for the 6D Coulomb system with $\delta = 0.01$. All methods show $O(\Delta t^2)$ convergence. Larger M reduces the error constant by $\sim 7 \times$ ($M=3$), $15 \times$ ($M=5$), $18 \times$ ($M=7$) relative to Strang. The splitting tests use complex64 arithmetic to fit the 29^6 arrays in GPU memory, and the reference ground state is computed in FP64.

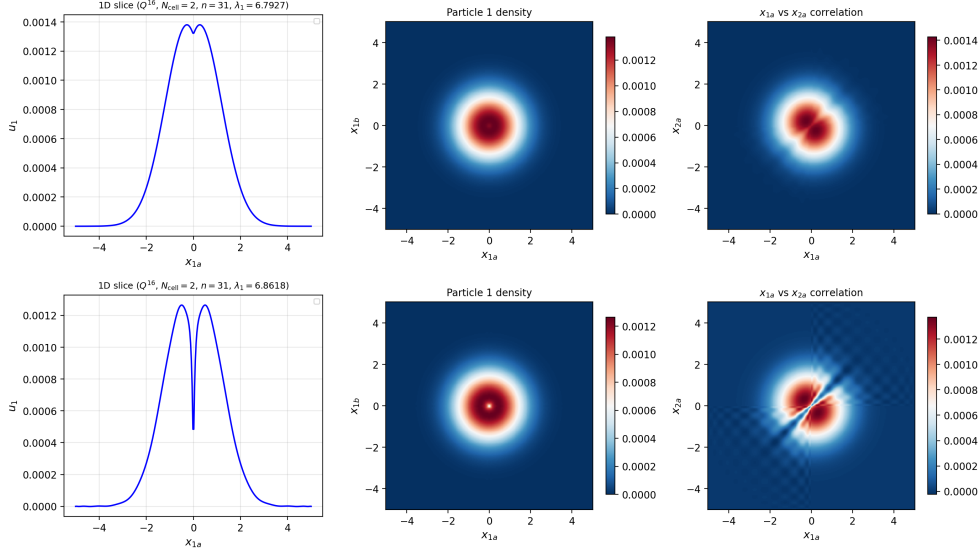


FIG. 6. Slices of the 6D Coulomb ground state at $31^6 \approx 8.9 \times 10^8$ DoFs, Q^{16} SEM, $N_{\text{cell}} = 2$, TF32, $L = 5$, GH200. Top: $\delta = 0.01$. Bottom: $\delta = 0.0001$. Left: 1D slice along x_{1a} . Center: particle 1 density. Right: inter-particle correlation x_{1a} vs. x_{2a} . Plotted on a 300×300 fine grid via cell-by-cell Q^{16} polynomial interpolation.

TABLE 14

$qHOP$ splitting error for the 6D Coulomb system (6.2), $\delta = 0.01$, Q^{10} SEM, 29^6 DoFs, complex64, $T=0.1$, GH200. t (s) is the GPU time.

Δt	$M = 1$ (Strang)			$M = 3$			$M = 5$			$M = 7$		
	Error	Rate	t (s)	Error	Rate	t (s)	Error	Rate	t (s)	Error	Rate	t (s)
0.1	1.98e-1	–	1.5	1.29e-1	–	2.2	1.75e-2	–	3.5	8.34e-3	–	3.6
0.02	9.76e-3	1.87	2.9	1.22e-3	2.90	5.8	4.87e-4	2.23	8.7	2.61e-4	2.15	12
0.005	5.51e-4	2.07	8.0	7.43e-5	2.02	19	3.00e-5	2.01	31	1.62e-5	2.01	43

EXAMPLE 6.4 (Order of approximated Magnus-2 in 6D, $\delta = 0.01$). Table 15 reports Magnus-2 via Yoshida with $M = 1, 3, 5, 7$. At large Δt , larger M reduces the error: at $\Delta t = 0.01$, the errors range from 7.93×10^{-4} ($M=1$) to 3.28×10^{-6} ($M=7$). At smaller Δt , the errors plateau at $\sim 2.5 \times 10^{-6}$ due to the complex64 arithmetic floor: with 20–50 time steps, single-precision rounding errors accumulate to $O(10^{-6})$.

6.3. Three particles in 3D with Coulomb interaction (9D). We consider three particles in 3D ($\mathbf{x}_1, \mathbf{x}_2, \mathbf{x}_3 \in \mathbb{R}^3$) in a harmonic trap with pairwise soft Coulomb interaction:

$$(6.3) \quad H = \sum_{j=1}^3 (-\Delta_{\mathbf{x}_j} + V_{\text{trap}}(\mathbf{x}_j)) + \sum_{1 \leq j < k \leq 3} \frac{c}{\sqrt{|\mathbf{x}_j - \mathbf{x}_k|^2 + \delta^2}},$$

where $V_{\text{trap}}(\mathbf{x}) = |\mathbf{x}|^2$. Discretized on $[-L, L]^3 \times [-L, L]^3 \times [-L, L]^3$ with Q^k SEM, this gives n^9 DoFs.

TABLE 15

Magnus-2 via Yoshida splitting error for the 6D Coulomb system (6.2), $\delta = 0.01$, Q^{10} SEM, 29^6 DoFs, complex64, $T=0.1$, GH200. $t(s)$ is the GPU time.

Δt	$M = 1$ (Yoshida)			$M = 3$			$M = 5$			$M = 7$		
	Error	Rate	t (s)	Error	Rate	t (s)	Error	Rate	t (s)	Error	Rate	t (s)
0.1	2.43e-1	–	2.3	1.78e-1	–	4.4	2.52e-1	–	6.0	2.72e-2	–	7.7
0.01	7.93e-4	2.49	12	1.55e-5	4.06	28	3.29e-6	4.88	46	1.99e-6	4.14	65
0.005	5.22e-5	3.93	22	2.34e-6 [†]	2.73	55	1.66e-6 [†]	0.99	91	2.77e-6 [†]	–0.48	128

[†]Error dominated by complex64 rounding accumulation.

6.3.1. Ground state. The offline eigendecomposition used in the separable preconditioner is computed in FP64, even though the online inverse iteration and PCG solves are carried out in FP32. The ground state is computed by shifted inverse iteration with $\sigma = 0$ and warm-start PCG (preconditioner $(\sum_j (-\Delta_{\mathbf{x}_j} + V_{\text{trap}}))^{-1}$, tolerance 10^{-4} with max 500 iterations). Warm-start uses the previous outer iteration's PCG solution as the initial guess for the next solve. Table 16 shows the ground state cost for $L = 3$, $c = 1$, Q^5 SEM, $N_{\text{cell}} = 2$, $n = 9$ ($9^9 \approx 3.9 \times 10^8$ DoFs) on GH200. PCG iterations increase with smaller δ , but all cases converge within 18 inverse iterations.

TABLE 16

Ground state of the 9D Coulomb Hamiltonian (6.3), 3 particles in 3D, Q^5 SEM, $N_{\text{cell}} = 2$, $9^9 \approx 3.9 \times 10^8$ DoFs, FP32, $\sigma = 0$, $L = 3$, GH200.

δ	V_C^{max}	Inv. iters	PCG solves	Time (s)	λ_1
0.01	100	18	110	490	11.7561
0.001	1000	18	349	588	11.9268
0.0001	10000	18	708	714	11.9502

Figure 7 shows slices of the ground state for two values of δ . As δ decreases, the Coulomb repulsion sharpens and the inter-particle anti-correlation pattern along $x_{1a} = x_{2a}$ becomes more pronounced.

6.3.2. Splitting convergence. The splitting $A = \sum_j (-\Delta_{\mathbf{x}_j} + V_{\text{trap}})$, $B = V_{12} + V_{13} + V_{23}$ is tested with $\delta = 0.1$, $T = 0.1$, complex64 arrays, using Q^5 SEM with $N_{\text{cell}} = 2$ ($n = 9$, $9^9 \approx 3.9 \times 10^8$ DoFs) on GH200. Errors of qHOP and Magnus-2 via Yoshida for $M = 1, 3, 5, 7$ are shown in Figure 8.

7. Concluding remarks. We extended the tensor-product solver of [28] from the Laplacian to $-\Delta + V$ on a single GPU, handling up to 10^9 DoFs in under one second. For non-separable potentials $V = V_1 + V_2$, the preconditioner $(-\Delta + V_1)^{-1}$ yields a preconditioned operator with a bounded condition number and spectrum clustering near 1, independently of the mesh size (Theorem 3.4), and also independently of the domain size when V_1 is confining and V_2 is bounded (Theorem 3.5). We applied this framework to ground state computation via shifted inverse iteration, PCG, and Gross–Pitaevskii gradient flows, and used the resulting eigenpairs as exact stationary solutions to validate the approximated versions of qHOP and Magnus-2 splitting methods at $\sim 10^8$ DoFs in 3D through 9D. The product-formula implementation showed the expected convergence orders and also provides a family of classical

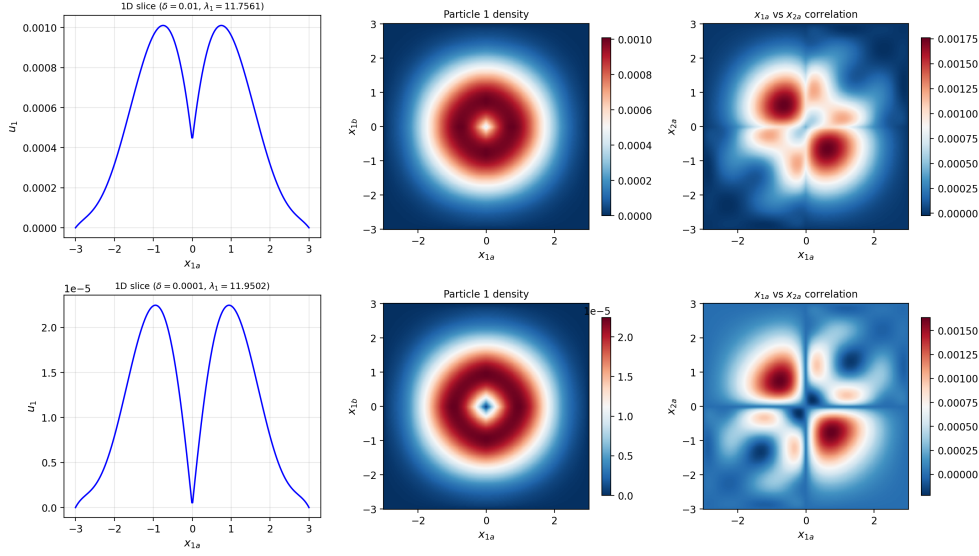


FIG. 7. Slices of the 9D Coulomb ground state, 3 particles in 3D, Q^5 SEM, 9^9 DoFs, FP32, $L = 3$, GH200. Top: $\delta = 0.01$. Bottom: $\delta = 0.0001$. Left: 1D slice along x_{1a} . Center: particle 1 density in the (x_{1a}, x_{1b}) plane. Right: x_{1a} vs. x_{2a} inter-particle correlation. Plotted on a 300×300 fine grid via cell-by-cell Q^5 polynomial interpolation.

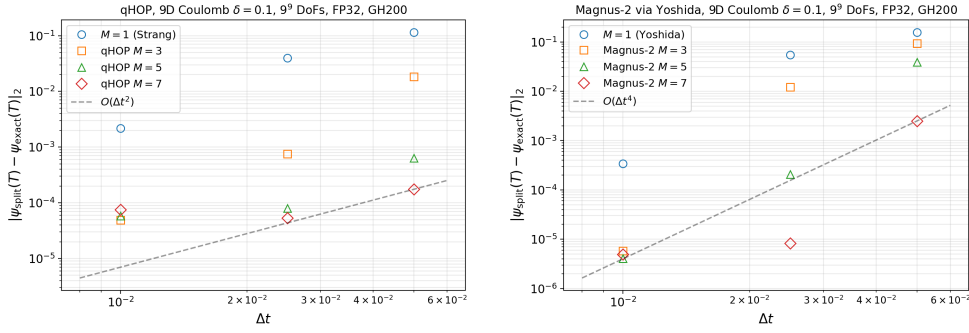


FIG. 8. Splitting convergence for 9D Coulomb, $\delta = 0.1$, $9^9 \approx 3.9 \times 10^8$ DoFs, complex64, FP64 transforms, $T = 0.1$, GH200. Left: qHOP ($O(\Delta t^2)$). Right: Magnus-2 via Yoshida ($O(\Delta t^4)$). Larger M reduces the error constant, and all methods hit the complex64 floor at $\sim 5 \times 10^{-6}$.

splitting methods generalizing second order Strang and fourth order Yoshida splittings.

Acknowledgments. The authors are grateful to Prof. Antoine Levitt at Laboratoire de Mathématiques d’Orsay, Université Paris-Saclay and Prof. Jianfeng Lu at Duke University for discussions on the Schrödinger operator. This work was partially supported by NSF DMS-2208518. This work used DeltaAI at the National Center for Supercomputing Applications (NCSA) through allocation MTH260013 from the Advanced Cyberinfrastructure Coordination Ecosystem: Services & Support (ACCESS) program, which is supported by U.S. National Science Foundation grants #2138259, #2138286, #2138307, #2137603, and #2138296.

Declaration of AI-assisted technologies. All original ideas, as well as the direct solver and PCG codes, are attributed to the authors. During the preparation of this work, the authors used Anthropic’s Claude Code to assist with mathematical discussions, further numerical implementation, and drafting of the manuscript. After using this tool, the authors carefully reviewed and edited the content as needed and take full responsibility for the final publication.

Appendix A. Hermite spectral method on unbounded domains.

The tensor-product solver of Section 2 applies to *any* discretization that produces a separable 1D operator $K = T\Lambda T^{-1}$ per axis. To illustrate this generality, we present the Hermite spectral method, which replaces the SEM on $[-L, L]^d$ with Hermite functions on \mathbb{R}^d , eliminating domain truncation artifacts for quantum systems in confining potentials. The n Hermite-Gauss nodes $\{x_j\}$ are eigenvalues of the $n \times n$ symmetric tridiagonal matrix J with $J_{k,k} = 0$ and $J_{k,k+1} = J_{k+1,k} = \sqrt{k/2}$ for $k = 1, \dots, n-1$. The Hermite function differentiation matrix at these nodes can be written as

$$D_{ij} = \frac{\psi_{n-1}(x_i)}{\psi_{n-1}(x_j)(x_i - x_j)}, \quad i \neq j, \quad D_{ii} = 0,$$

where ψ_{n-1} is the normalized Hermite function of degree $n-1$. See [34, Eq. (7.93)]. Given a separable potential $f(x)$, the 1D operator is $K = -D^2 + \text{diag}(f(x_j))$, with eigendecomposition $K = T\Lambda T^{-1}$. The d -dimensional tensor-product solver is identical to SEM. No boundary conditions are needed, since the Hermite functions decay as $e^{-x^2/2}$. The method is limited to $n \lesssim 745$ in FP64 due to underflow in the Hermite function recurrence at the outermost nodes. Table 17 shows the accuracy of $(-\Delta + V)^{-1}$ on \mathbb{R}^3 with the potential (2.6). Figure 9 shows that the proposed preconditioner $(-\Delta + V_1)^{-1}$ converges in 5 PCG iterations on \mathbb{R}^3 , while the baseline P_C does not converge within 500 iterations. Table 18 reports the Magnus-2 convergence using the Hermite spectral method with separable potential (4.1), 499³ DoFs, $T = 1$. For $M \geq 3$, the observed convergence is $O(\Delta t^4)$.

TABLE 17

Accuracy for using $(-\Delta + V)^{-1}$ to solve $(-\Delta + V)u = f$ with potential (2.6) on \mathbb{R}^3 via Hermite spectral method, FP64, A100. The exact solution is $u^* = \frac{\sin(\frac{\pi}{2}(x+1))}{1+x^2} \cdot \frac{\sin(\pi(y+1))}{1+y^2} \cdot \frac{\sin(\frac{3\pi}{2}(z+1))}{1+z^2}$.

n	DoFs	Setup (s)	Solve (s)	Weighted L^2 err	ℓ^2 rel. err
199	199 ³	2.7	0.002	1.53×10^{-5}	6.31×10^{-5}
399	399 ³	3.2	0.024	4.05×10^{-6}	2.20×10^{-5}
599	599 ³	3.2	0.117	1.87×10^{-6}	1.20×10^{-5}

TABLE 18

Approximated Magnus-2, Hermite spectral on \mathbb{R}^3 , 499³ DoFs, complex128, $T=1$, GH200. t (s) is the GPU time.

Δt	Yoshida ($M = 1$)			Magnus-2 $M = 3$			Magnus-2 $M = 5$			Magnus-2 $M = 7$		
	Error	Rate	t (s)	Error	Rate	t (s)	Error	Rate	t (s)	Error	Rate	t (s)
0.2	1.34e+0	–	1.7	1.41e+0	–	11	3.05e-1	–	16	1.11e-1	–	23
0.125	1.21e+0	0.22	2.7	4.85e-1	2.27	17	3.59e-2	4.55	26	8.85e-3	5.38	36
0.1	1.52e+0	-1.02	3.4	1.11e-1	6.61	21	1.26e-2	4.69	33	3.51e-3	4.14	45
0.05	5.48e-1	1.47	6.7	5.17e-3	4.42	42	7.60e-4	4.05	65	2.22e-4	3.98	91

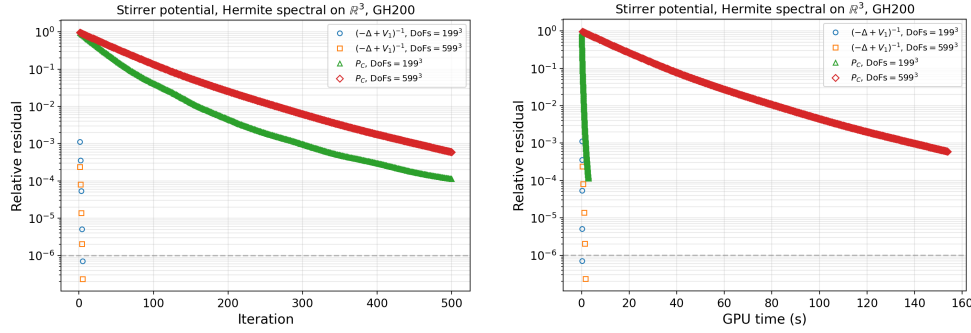


FIG. 9. PCG convergence with Hermite spectral method on \mathbb{R}^3 . Stirrer potential, FP32, GH200.

REFERENCES

- [1] D. AN, D. FANG, AND L. LIN, *Time-dependent Hamiltonian simulation of highly oscillatory dynamics and superconvergence for Schrödinger equation*, *Quantum*, 6 (2022), p. 690.
- [2] X. ANTOINE AND R. DUBOSCQ, *Modeling and computation of Bose–Einstein condensates: stationary states, nucleation, dynamics, stochasticity*, in *Nonlinear Optical and Atomic Systems: At the Interface of Physics and Mathematics*, Springer International Publishing, 2015, pp. 49–145.
- [3] X. ANTOINE, A. LEVITT, AND Q. TANG, *Efficient spectral computation of the stationary states of rotating Bose–Einstein condensates by preconditioned nonlinear conjugate gradient methods*, *J. Comput. Phys.*, 343 (2017), pp. 92–109.
- [4] W. BAO AND Q. DU, *Computing the ground state solution of Bose–Einstein condensates by a normalized gradient flow*, *SIAM J. Sci. Comput.*, 25 (2004), pp. 1674–1697.
- [5] W. BAO, S. JIN, AND P. A. MARKOWICH, *On time-splitting spectral approximations for the Schrödinger equation in the semiclassical regime*, *J. Comput. Phys.*, 175 (2002), pp. 487–524.
- [6] T. J. BOERNER, S. DEEMS, T. R. FURLANI, S. L. KNUTH, AND J. TOWNS, *ACCESS: Advancing innovation: NSF’s advanced cyberinfrastructure coordination ecosystem: Services & support*, in *Practice and Experience in Advanced Research Computing 2023: Computing for the Common Good*, 2023, pp. 173–176.
- [7] Y. BORNS-WEIL, D. FANG, AND J. ZHANG, *Discrete superconvergence analysis for quantum Magnus algorithms of unbounded Hamiltonian simulation*, *Commun. Math. Phys.*, 407 (2026), p. 29.
- [8] M. CALIARI, F. CASSINI, L. EINKEMMER, A. OSTERMANN, AND F. ZIVCOVICH, *A μ -mode integrator for solving evolution equations in Kronecker form*, *J. Comput. Phys.*, 455 (2022), p. 110989.
- [9] Z. CHEN, J. LU, Y. LU, AND X. ZHANG, *Fully discretized Sobolev gradient flow for the Gross–Pitaevskii eigenvalue problem*, *Math. Comp.*, 94 (2025), pp. 2723–2760.
- [10] A. M. CHILDS, J. LENG, T. LI, J.-P. LIU, AND C. ZHANG, *Quantum simulation of real-space dynamics*, *Quantum*, 6 (2022), p. 860.
- [11] I. DANAILA AND B. PROTAS, *Computation of ground states of the Gross–Pitaevskii functional via Riemannian optimization*, *SIAM J. Sci. Comput.*, 39 (2017), pp. B1102–B1129.
- [12] D. FANG, D. LIU, AND R. SARKAR, *Time-dependent Hamiltonian simulation via Magnus expansion: Algorithm and superconvergence*, *Commun. Math. Phys.*, 406 (2025), p. 128.
- [13] D. FANG, X. WU, AND A. SOFFER, *On the Trotter error in many-body quantum dynamics with Coulomb potentials*, *Commun. Math. Phys.*, 407 (2026), p. 83.
- [14] D. FANG AND J. ZHANG, *Superconvergence of high-order Magnus quantum algorithms*, 2025. arXiv:2509.22897.
- [15] X. FENG, H. H. S. CHAN, AND D. P. TEW, *Improved grid-based simulation of Coulombic dynamics*, 2026. arXiv:2603.02954.
- [16] I. K. GAINULLIN AND M. A. SONKIN, *High-performance parallel solver for 3D time-dependent Schrödinger equation for large-scale nanosystems*, *Comput. Phys. Commun.*, 188 (2015), pp. 68–75.
- [17] A. HAHN, P. HARTUNG, D. BURGARTH, P. FACCHI, AND K. YUASA, *Lower bounds for the Trotter error*, *Phys. Rev. A*, 111 (2025), p. 022417.

- [18] D. B. HAIDVOGEL AND T. ZANG, *The accurate solution of Poisson's equation by expansion in Chebyshev polynomials*, J. Comput. Phys., 30 (1979), pp. 167–180.
- [19] W. HAO, S. LEE, AND X. ZHANG, *An efficient quasi-Newton method with tensor product implementation for solving quasi-linear elliptic equations and systems*, J. Sci. Comput., 103 (2025), p. 89.
- [20] P. HENNING AND D. PETERSEIM, *Sobolev gradient flow for the Gross–Pitaevskii eigenvalue problem: Global convergence and computational efficiency*, SIAM J. Numer. Anal., 58 (2020), pp. 1744–1772.
- [21] M. HOCHBRUCK AND C. LUBICH, *On Magnus integrators for time-dependent Schrödinger equations*, SIAM J. Numer. Anal., 41 (2003), pp. 945–963.
- [22] B. JACKSON, J. F. MCCANN, AND C. S. ADAMS, *Vortex formation in dilute inhomogeneous Bose–Einstein condensates*, Phys. Rev. Lett., 80 (1998), pp. 3903–3906.
- [23] T. JAHNKE AND C. LUBICH, *Error bounds for exponential operator splittings*, BIT Numer. Math., 40 (2000), pp. 735–744.
- [24] S. JIN, P. A. MARKOWICH, AND C. SPARBER, *Mathematical and computational methods for semiclassical Schrödinger equations*, Acta Numer., 20 (2011), pp. 121–209.
- [25] Y.-Y. KWAN AND J. SHEN, *An efficient direct parallel spectral-element solver for separable elliptic problems*, J. Comput. Phys., 225 (2007), pp. 1721–1735.
- [26] C. LASSER AND C. LUBICH, *Computing quantum dynamics in the semiclassical regime*, Acta Numer., 29 (2020), pp. 229–401.
- [27] H. LI, D. APPELÖ, AND X. ZHANG, *Accuracy of spectral element method for wave, parabolic, and Schrödinger equations*, SIAM J. Numer. Anal., 60 (2022), pp. 339–363.
- [28] X. LIU, J. SHEN, AND X. ZHANG, *A simple GPU implementation of spectral-element methods for solving 3D Poisson type equations on rectangular domains and its applications*, Commun. Comput. Phys., 36 (2024), pp. 1157–1185.
- [29] R. E. LYNCH, J. R. RICE, AND D. H. THOMAS, *Direct solution of partial difference equations by tensor product methods*, Numer. Math., 6 (1964), pp. 185–199.
- [30] J. E. OSBORN, *Spectral approximation for compact operators*, Math. Comp., 29 (1975), pp. 712–725.
- [31] M. REED AND B. SIMON, *Methods of Modern Mathematical Physics, Vol. I: Functional Analysis*, Academic Press, New York, 1972.
- [32] ———, *Methods of Modern Mathematical Physics, Vol. IV: Analysis of Operators*, Academic Press, New York, 1978.
- [33] J. SHEN, *Efficient spectral-Galerkin method I. Direct solvers of second- and fourth-order equations using Legendre polynomials*, SIAM J. Sci. Comput., 15 (1994), pp. 1489–1505.
- [34] J. SHEN, T. TANG, AND L.-L. WANG, *Spectral Methods: Algorithms, Analysis and Applications*, vol. 41 of Springer Series in Computational Mathematics, Springer, Heidelberg, 2011.
- [35] Y. SU, H.-Y. HUANG, AND E. T. CAMPBELL, *Nearly tight Trotterization of interacting electrons*, Quantum, 5 (2021), p. 495.
- [36] M. THALHAMMER, *High-order exponential operator splitting methods for time-dependent Schrödinger equations*, SIAM J. Numer. Anal., 46 (2008), pp. 2022–2038.
- [37] A. VAN DER SLUIS AND H. A. VAN DER VORST, *The rate of convergence of conjugate gradients*, Numer. Math., 48 (1986), pp. 543–560.
- [38] H. YOSHIDA, *Construction of higher order symplectic integrators*, Phys. Lett. A, 150 (1990), pp. 262–268.